

Meter-scale slopes of candidate MER landing sites from point photogrammetry

Ross A. Beyer and Alfred S. McEwen

Department of Planetary Sciences, The University of Arizona, Tucson, Arizona, USA

Randolph L. Kirk

Astrogeology Team, U.S. Geological Survey, Flagstaff, Arizona, USA

Received 13 May 2003; revised 16 July 2003; accepted 22 August 2003; published 4 December 2003

An edited version of this paper was published by AGU. Copyright © 2003 American Geophysical Union. For more information about the details, see Appendix B of this paper.

Photogrammetry was used to analyze the small-scale roughness of areas that fall within the proposed Mars Exploration Rover (MER) 2003 landing ellipses. The landing ellipses presented in this study were those in Athabasca Valles, Elysium Planitia, Eos Chasma, Gusev Crater, Isidis Planitia, Melas Chasma, and Meridiani Planum. We were able to constrain surface slopes on length scales comparable to the image resolution (1.5 to 12 meters/pixel). The MER 2003 mission has various engineering constraints that each candidate landing ellipse must satisfy. These constraints indicate that the statistical value of the slopes at 5 m baselines are an important criterion. We used our technique to constrain maximum surface slopes across large swaths of each image, and built up slope statistics for the images in each landing ellipse. We are confident that all MER 2003 landing site ellipses in this study, with the exception of the Melas Chasma ellipse, are within the small-scale roughness constraints. Our results have provided input into the landing hazard assessment process. In addition to evaluating the safety of the landing sites, our mapping of small-scale roughnesses can also be used to better define and map morphologic units. The morphology of a surface is characterized by the slope distribution and magnitude of slopes. In looking at how slopes are distributed, we can better define landforms and determine the boundaries of morphologic units.

INDEX TERMS: Planetology: Solid Surface Planets: Remote sensing; Planetology: Solid Surface Planets: Surface materials and properties; Planetology: Solid Surface Planets: Instruments and techniques.

KEYWORDS: Mars, 2003 Mars Exploration Rovers, photogrammetry, landing sites.

Citation: Beyer, R. A., A. S. McEwen, and R. L. Kirk, Meter-scale slopes of candidate MER landing sites from point photogrammetry, *J. Geophys. Res.*, 108(E12), 8085, doi:10.1029/2003JE002120, 2003. To view the published open abstract, go to <http://dx.doi.org> and enter the DOI.

1 Introduction

The Mars Exploration Rover (MER) mission (*Crisp et al.*, 2003) will be sending two rovers to the surface of Mars in early 2004. In order to reduce the risks of damage during landing, the MER project has determined a set of engineering constraints (*Golombek et al.*, 2003) that potential landing ellipses must satisfy. Among these constraints are those which indicate that the percentage of slopes greater than 15 degrees should be minimized. The MER 2003 project had a short list of seven landing ellipses that they had identified for further study, and two of those sites have been selected as landing sites for the MER rovers, the Gusev Crater site and the Meridiani Planum site.

The engineering constraints identify slopes on two length scales that are relevant to the mission. On length scales of hundreds of meters, a shallow slope would cause increased rolling velocity once the air-bag enveloped lander touches down, and would cause increased bouncing across the surface. Steeper slopes may also contribute to fooling the landing altimeter, causing either early or late rocket firing, dubbed the “mesa” failure scenario. On length scales of several meters, the size of the spacecraft, steep slopes may affect rover deployment and mobility, but also may cause added or increased bouncing.

The Mars Orbiter Laser Altimeter (MOLA) (*Smith et al.*, 2001) data are ideal for determining slopes on length scales greater than the instrument’s shot-to-shot distance which is about 300 m along track and ~ 1 km between tracks at the equator, and has been used to constrain landing site selection (*Haldemann and Anderson*, 2002; *Golombek et al.*, 2003). Each MOLA shot also contains information about the roughness within the instrument’s footprint via the measured width of the returned pulse. However, this roughness information has a length scale of about 75 m (*Neumann et al.*, 2003; *Garvin et al.*, 1999).

The best data set available to evaluate surface slopes on the scale of meters is that of the Mars Orbiter Camera (MOC) (*Malin and Edgett*, 2001). We use a point photogrammetry technique to analyze calibrated narrow angle MOC images that complements and extends the area photogrammetry and stereogrammetry work by *Kirk et al.* (2003). Our point photogrammetry method allows us to obtain many slope measurements on all available MOC images and to build up statistics for the images that are

in a given landing ellipse. This technique is a significant advance over qualitative evaluation of surface roughness. Our method normalizes the photometry for emission and incidence angles. Our results avoid misleading qualitative evaluations when the pixels of an image are scaled to increase contrast, or “stretched”.

The MOC images used in this study were mostly taken at a local solar time of ~ 2 P.M., but incidence angles vary from 20 to 70 degrees. Additionally, most MOC images are nadir-looking and despite some off-nadir pointing for the images in our study, the emission angles are mostly near zero degrees.

Early in the site selection process this study began with twenty-six candidate landing ellipses, but we will only present information on the seven landing ellipses that made it to the latter stages of the site selection process as well as calibration measurements of the Viking and Pathfinder landing sites. Any of these sites may be reconsidered for future landers.

2 Method

Photogrammetry, or shape-from-shading, is the general technique of obtaining slopes or topography from the brightness values in an image. It can be applied in a number of different ways depending on how the individual brightness values of the pixels are integrated together (or not) and how ambiguity in slope azimuth is resolved to produce final slope values for those pixels. The term “ n -dimensional photogrammetry” is used where n refers to the dimensionality of the region over which information is built up.

The photogrammetry method that we primarily use in this study is that of “point” photogrammetry. We are measuring the brightness of a single pixel to yield a slope measurement, and we in turn take these point measurements of slope and perform statistical analyses directly on them.

When slope information from individual points along a line is modeled, and the result is a height profile, this is known as “profiling” photogrammetry, or one-dimensional photogrammetry. Similarly, when slope information from many points in a grid (or a square region on an image) are modeled, and the result is a topographic surface, this is known as “area” photogrammetry, or two-dimensional pho-

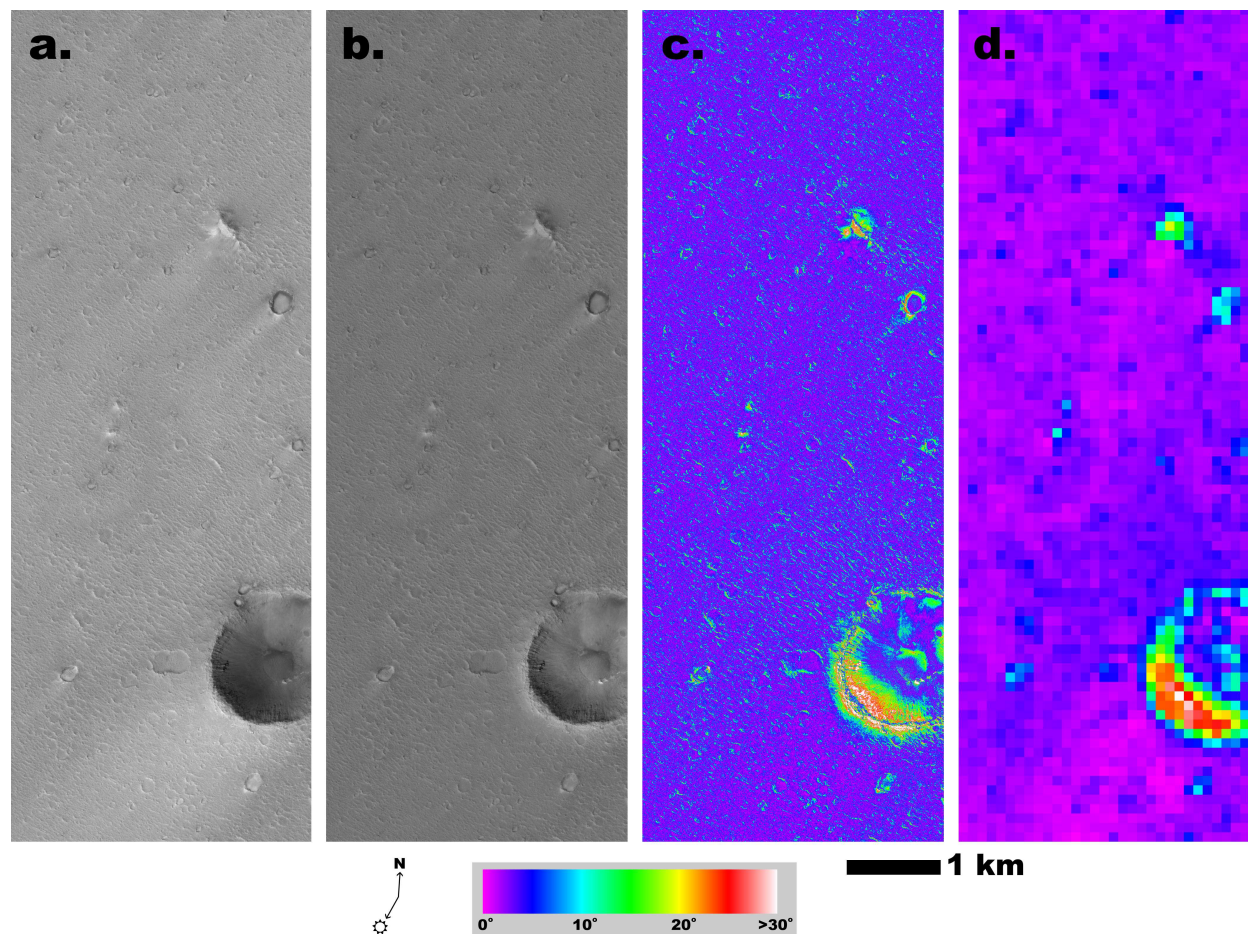


Figure 1: These figures contain an example of the processing done in this study. This image is M11/02414, the Pathfinder landing site is on this image. (a) This image has undergone initial calibration and aspect ratio correction (ISIS Level 1). (b) Haze removal and divide boxcar filtering result in this image. (c) Absolute value of the slope image. (d) RMS slope image at 100 m/pixel.

toclinometry. This terminology can be confusing since two-dimensional photoclinometry yields three-dimensional topographic information.

2.1 Image Processing

All MOC images that we used have been calibrated with the United States Geological Survey’s Integrated Software for Imagers and Spectrometers (ISIS version 010515) (e.g. *Eliason et al.*, 2001; *Gaddis et al.*, 1997). Initial processing of the images involved ingestion of the raw Planetary Data System (PDS) format images, elimination of obviously bad or corrupted pixels, and radiometric calibration. Many images have coarser down-track reso-

lution than cross-track resolution, i.e. pixels do not represent a “square” area on the surface of Mars. In order to compensate for this and to preserve as much original pixel information as possible, we enlarged the image in the down-track direction such that the resolutions in the down-track and cross-track directions were the same. Most of the photometric information that we require for our technique, such as image resolution, incidence angle, and emission angle, was extracted from the labels of the calibrated images, which were derived from the SPICE data (e.g. *Acton*, 1996, 1999).

Slope statistics vary strongly with spatial scale (*Shepard et al.*, 2001), so we needed to normalize

Slopes from Point Photoclinometry vs. Exact Values, Uniform Albedo

"Sun" Azimuth (degrees from sample axis)	Hurst		Exact RMS Slope		Point PC RMS Slope		Point PC/Exact Ratio	
	Exponent H	Filter	pixel centers	pixel edges	$L = 0.55$	$k = 0.72$	$L = 0.55$	$k = 0.72$
0°	0.2		1.00°	1.76°	1.76°	1.68°	0.9980	0.9527
	0.5		1.00°	1.62°	1.62°	1.54°	0.9999	0.9505
	0.8		1.00°	1.37°	1.38°	1.31°	1.0040	0.9531
	0.8	Highpass	0.90°	1.30°	1.31°	1.24°	1.0047	0.9510
	0.8	Lowpass	0.52°	0.52°	0.52°	0.50°	1.0002	0.9617
	0.8		9.99°	13.74°	13.62°	13.05°	0.9910	0.9496
22.5°	0.2		1.00°	1.76°	1.77°	1.68°	1.0037	0.9527
	0.5		1.00°	1.62°	1.62°	1.54°	0.9999	0.9505
	0.8		1.00°	1.37°	1.37°	1.31°	0.9967	0.9531
	0.8	Highpass	0.90°	1.30°	1.31°	1.25°	1.0047	0.9587
	0.8	Lowpass	0.52°	0.52°	0.52°	0.49°	1.0002	0.9425
	0.8		9.99°	13.74°	13.43°	12.88°	0.9772	0.9372

Table 1: This table shows how the point photoclinometry that we use in this study performs on synthetic fractal terrain illuminated from two different directions. The column labeled "Exact RMS Slope" has two columns, one for the down-sun RMS slopes measured between pixel centers, and one for the down-sun RMS slopes measured between pixel edges. "PC" is used as an abbreviation for photoclinometry. There are also two columns for the down-sun slope measured with our point photoclinometry technique. One using a lunar-Lambert photometric function with $L = 0.55$ to illuminate the topography, and the other using a Minnaert photometric function with $k = 0.72$. The down-sun RMS slopes are derived from our point photoclinometry method by using a lunar-Lambert photometric function with $L = 0.55$ in both instances. The "Point PC/Exact Ratio" column is a ratio of the results from our point photoclinometry technique and dividing them by the exact down-sun RMS slope from the pixel edges of the synthetic topography images.

slope statistics measured from images with different resolutions. In order to facilitate this, we found that most of the images near the landing site ellipses had resolutions better than 6 meters per pixel, and so all images were degraded to that resolution. Doing this averages pixel information together, which potentially mixes slope information from many surfaces together, but it also increases the effective baseline over which slopes are measured. These two things together don't significantly contribute to errors in the slopes at these length scales. We explore the variation of slope information with baseline in Section 2.3.3.

Our technique measures the slope of each pixel directly. We do not produce a profile of heights in the down-sun direction, and therefore we completely avoid the cumulative elevation errors involved in profiling photoclinometry. Similarly we are not solving for a smoothed topographic surface like area photoclinometry does. Despite these differences, our technique does share the three major sources of error for photoclinometry that other techniques suffer from: haze, albedo variations, and determination of slope azimuth.

2.1.1 Haze Compensation

The Martian atmosphere scatters incident sunlight towards the camera and onto the surface, where it acts as a diffuse illumination source that brightens the image while contributing minimally to topographic shading. Additionally, there must be some scattered light within the MOC camera itself and an offset calibration residual within each image. We think of these factors together as a uniform brightness contribution to the image, or "haze" in the scene. This has an effect on the observed topography which causes both the human eye and our photoclinometry algorithm to misinterpret the value of the slopes. Therefore, we must find an estimate of the haze for each image, and subtract it from the brightness values so that our algorithm does not report gentle slopes where the true slopes are steeper.

Ideally, there would be some independent measure of the haze. For example, if the amplitude of the topography is known from another method such as stereogrammetry, then the haze value can be adjusted until the slopes reported by photoclinometry matched those of the topography from stereogram-

Slopes from Point Photoclinometry vs. Exact Values, Non-Uniform Albedo

"Sun" Azimuth (degrees from sample axis)	Hurst Exponent H	Fractional Albedo Variation	Exact RMS Slope		Point PC RMS Slope		Point PC/Exact Ratio	
			pixel centers	pixel edges	$L = 0.55$	$k = 0.72$	$L = 0.55$	$k = 0.72$
0°	0.8	0	1.00°	1.37°	1.37°	1.31°	0.9940	0.9531
	0.8	0.0063	1.00°	1.37°	1.47°	1.41°	1.0704	1.0258
22.5°	0.8	0	1.00°	1.37°	1.39°	1.31°	1.0110	0.9531
	0.8	0.0063	1.00°	1.37°	1.47°	1.40°	1.0664	1.0186

Table 2: This table shows how the point photoclinometry that we use in this study performs on the synthetic fractal terrain when albedo variations are added to the artificial surface. With the exception of the "Fractional Albedo Variation" column, the columns are identical to those in Table 1.

metry or altimetry (e.g. *Kirk et al.*, 2003; *Soderblom et al.*, 2002). This approach is not feasible for the present work because our goal is to make photoclinometric slope estimates over much larger areas than can be mapped in stereo. Another way to measure the haze would be to directly estimate it from infrared data. We have found that Viking IRTM opacity estimates provide a consistent lower bound on atmospheric opacities derived from shadows in Viking Orbiter images, but frequently underestimate the visible opacity, so the IR data are not useful for calibrating photoclinometry directly (*Kirk et al.*, 2001).

Another way to gain an estimate of the haze in an image would be to search for true shadows in average-albedo regions in the image and use the DN (data number) value within those areas as the haze value. Using shadows as haze estimators in this way introduces some error since shadows do not have a fixed brightness. The directionality of skylight means that shadow brightnesses vary with how much of the sky the surface sees, but this effect is only on the order of tens of percent (*Kirk et al.*, 2001). A more significant problem for our work is that the 2 P.M. mean local time of the images means that only very steep slopes (greater than $\sim 60^\circ$) would cast true shadows. In addition, manual searching for believable shadows is quite time-consuming. In order to speed the process for the more than one hundred images in this study, we decided to use the minimum pixel value in each scene as the haze value to subtract. If there are no shadows in the image, this darkest pixel may simply be a low-albedo region of the surface, in which case using its brightness overestimates the true haze value of the scene. This provides a good upper limit to the slopes, because overestimating the haze results in measured slopes that will be steeper than the actual slopes.

An advantage of performing our technique on a number of images in the same area is that occasionally an image had anomalously steep model slopes when compared to images of similar or identical terrain. When this happened, we could tell that the automatic haze estimate was quite large, and it could be scaled back to bring the slope statistics of the image into better agreement with other images in the area. Consistency between images does not necessarily mean that an accurate haze estimate has been found, merely that the darkest pixel in each image is comparable.

2.1.2 Compensation for Albedo Variations

Photoclinometry interprets light and dark shading in the scene as slopes on a surface of uniform albedo. If there are patches of significantly darker or lighter material than the majority of the scene, then the photoclinometry algorithm will misinterpret those variations as resulting from topography. Unfortunately, this is quite difficult to compensate for. Albedo variations commonly persist over large areas whereas there's a limit to how much dark or bright slopes do so, therefore broad changes in brightness are more likely to be albedo and it is helpful to filter such broad changes.

In order to minimize the effect of albedo variations and large-scale topography on our measurements, we applied a divide boxcar filter on the image such that the resultant pixels are $D(i, j) = P(i, j)/(S(i, j)/N(i, j))$ where $P(i, j)$ is the original value of the pixel at the i, j location, $S(i, j)$ is the sum of valid points over the box centered at i, j , and $N(i, j)$ is the number of valid points in that box. The size of the boxcar filter was 600 m on a side, which is roughly equivalent to twice the MOLA shot spacing at the surface near the equator. This filter-

ing effectively removes any topographic shading and albedo effects at scales greater than 600 m. MOLA data for the terrain in these landing ellipses indicated that the regional slopes for these areas were flat, and we therefore didn't feel the need to re-insert the MOLA regional slopes for our results. However, this boxcar filtering of the image only normalizes large scale albedo variations, and small scale albedo variations cannot be completely eliminated. An example of an image with initial calibration, automatic haze removal, and boxcar filtering can be found in Figures 1a and 1b.

One way to eliminate small scale albedo differences would be to take advantage of the fact that they are often correlated with color. However, the narrow-angle MOC camera is monochromatic, color differences between dark and bright materials on Mars are subtle, and the martian skylight is colored, so shadows are differently colored as well. For this study, the best way to minimize the problem is to utilize the complex image processing apparatus of the human eye/brain system to identify and avoid images, or regions of images, where severe albedo variations are visually evident.

Small-scale albedo variations that remain within images will cause the slope models to be steeper than they truly are. However, we still derive robust upper limits to slope angles.

2.1.3 Slope Azimuth

The azimuth, or dip direction, of slopes in real terrain will be oriented in various directions. The difficulty is in determining what that azimuth is. If the azimuth of a given slope is not specified, then there isn't a unique brightness for that slope. The work of *Kirk et al.* (2003) and other area photoclinometry techniques numerically model the azimuth of the slope and the value of the slope itself.

Our technique assumes a very simple geometry in which the azimuth of the model slopes we measure are constrained to be in the direction of solar illumination. Therefore the Sun, the spacecraft, and the portion of the surface imaged define a plane. It is within this plane that we obtain our model slopes. This constraint allows us to have a unique relationship between a given slope and a given brightness. However, since true slopes have a variety of azimuths, we are only measuring the true slope if its azimuth is in the down-sun direction. For the most part, the azimuths of true slopes will not be in the

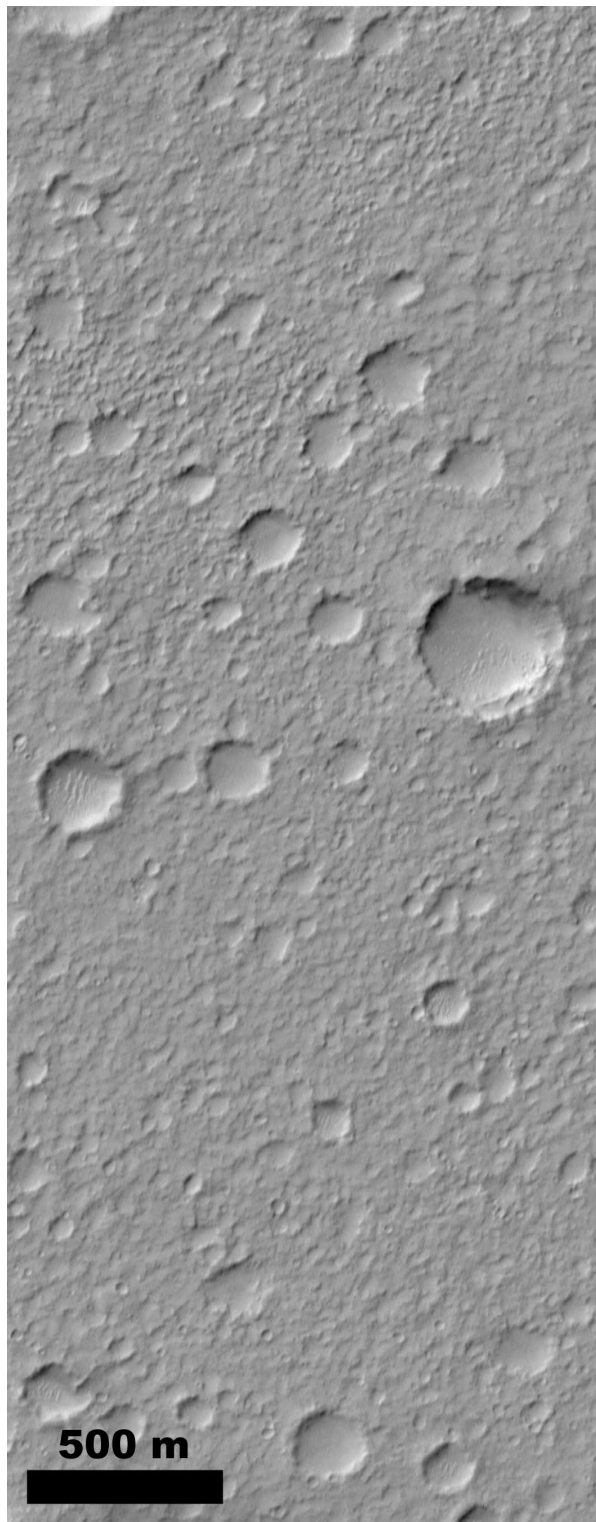


Figure 2: Portion of MOC image E02/00665 in Gusev Crater, referred to as image *Gusev 1d* by *Kirk et al.* (2003) and in this paper.

down-sun direction, and this assumption of azimuth will cause this technique to report a slope shallower than the true slope.

This is the only key assumption in our technique that underestimates the value of the true slopes. We have evaluated this error for fractal topography, as discussed below in Section 3.1, and found it to be only about 2% when compared to bidirectional slopes measured from the fractal topography. This error is less than 1% for the smooth surfaces typical of the MER landing sites. This error would be larger if the slope azimuths had a systematic orientation orthogonal to the down-sun direction.

The measurements from our technique result in bidirectional slopes in the down-sun direction. In order to obtain an approximation of the adirectional slopes, one could assume that the slope distribution is isotropic and Gaussian in which case the adirectional slope distribution would be a factor of $\sqrt{2}$ greater than the bidirectional value (*Shepard et al.*, 2001). *Kirk et al.* (2003) explicitly calculate the ratio of the adirectional root mean square (RMS) and bidirectional RMS slopes based on their data, and find empirically that this ratio is constant and nearly equal to $\sqrt{2}$. This is a statistical relation over an area that is large compared to the topographic features that contribute to the slopes.

2.2 Photometry

We start with a lunar-Lambert photometric function after *McEwen* (1991, 1986) of the form

$$I(\mu, \mu_0, \alpha) = Bo(\alpha) \left[\frac{2L(\alpha)\mu_0}{\mu + \mu_0} + (1 - L(\alpha))\mu_0 \right] \quad (1)$$

Where $I(\mu, \mu_0, \alpha)$ is the reflectance function, μ is the cosine of the emission angle ϵ , μ_0 is the cosine of the incidence angle ι , α is the phase angle, $Bo(\alpha)$ is the intrinsic albedo or the value of $I(1, 1, \alpha)$, and $L(\alpha)$ is equal to $Af(\alpha)/[Af(\alpha) + 2B]$, as defined by *McEwen* (1991). The above equation can be simplified if we create a ratio of the brightness value of some topography with slope θ to the brightness of flat topography:

$$\frac{I^*}{I} = \frac{\frac{2L(\alpha)\mu_0^*}{\mu^* + \mu_0^*} + (1 - L(\alpha))\mu_0^*}{\frac{2L(\alpha)\mu_0}{\mu + \mu_0} + (1 - L(\alpha))\mu_0} \quad (2)$$

This leaves us with two unknowns (the values of μ^* and μ_0^* for the tilted terrain) to be solved for given

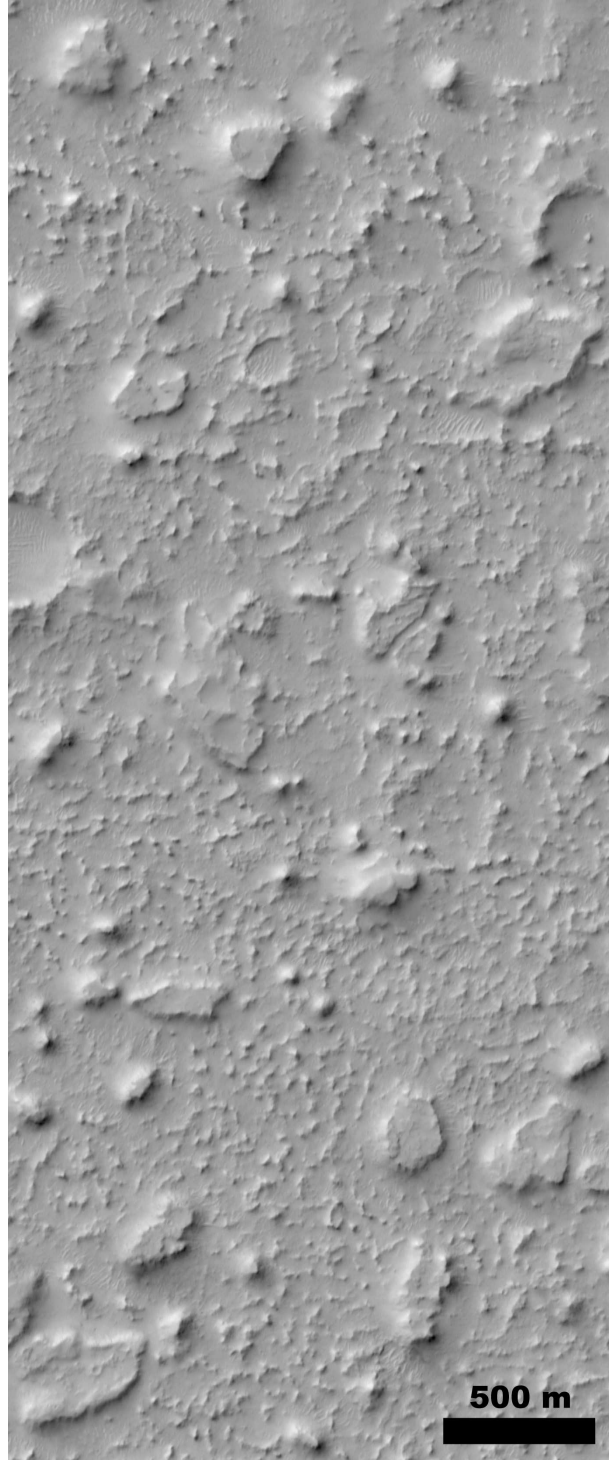


Figure 3: Portion of MOC image E02/00665 in Gusev Crater, referred to as image *Gusev 1e* by *Kirk et al.* (2003) and in this paper.

Point Photoclinometry Slopes vs. Area Photoclinometry for MOC Images

MOC Image			Darkest	<i>Kirk et al.</i>	Point PC RMS Slope	
Region	Description	<i>Kirk et al.</i>	Pixel	Area PC	<i>Kirk et al.</i>	Darkest
		Haze	Value	RMS Slope	Haze	Pixel Haze
E02/00665						
Gusev 1d	Cratered plains, albedo variations minimal	0.087	0.120	4.20°	4.20°	7.59°
Gusev 1e	Knobby etched plains, albedo variations minimal	0.087	0.085	9.35°	8.87°	8.53°
E03/01763						
Hematite 2a	Smooth plains, albedo variations severe	0.086	0.157	3.10°	2.06°	6.56°
Hematite 2b	Smooth plains, albedo variations moderate	0.086	0.175	1.25°	1.04°	8.04°
Hematite 2c	Plains with rougher outcrops albedo variations moderate	0.086	0.178	2.21°	2.46°	16.80°

Table 3: This table shows the comparison between the down-sun slopes of the *Kirk et al.* (2003) area photoclinometry, and the down-sun slopes of this study’s point photoclinometry on the same image regions. This table also shows the results of point photoclinometry using both the more precise haze estimates of *Kirk et al.* (2003), and the darkest pixel haze values that we use in this study. The region names that are used here are the same names as those used and defined by *Kirk et al.* (2003).

the value of the ratio I^*/I . These two unknowns can be reduced to one under the assumption, discussed above, that local surface slopes are always in the up- or down-sun direction. For each pixel in the image, we wish to know the angle, θ , at which the surface is tilted with respect to a flat surface (positive if tilted towards the light source). Since $\mu_0 = \cos(\iota)$ and $\mu = \cos(\epsilon)$, we seek $\mu_0^* = \cos(\iota - \theta)$ and μ^* . With the further simplifying assumption that not only the surface slope direction but also the spacecraft lies in the same plane as the sun, we have $\mu^* = \cos(\epsilon \pm \theta)$. Imagine a line that is the projection of the normal vector of the surface being imaged onto this plane. The negative sign then applies when the spacecraft is on the same side of this vertical as the sun, and the positive sign when it is on the opposite side of the vertical. It is important to note that this expression for μ^* is strictly valid when the emission direction is in the plane defined by the sun, but will be approximately valid when the emission direction is not far from that plane, in particular, when the emission angle itself is small. Most of the MOC images used in this study have emission angles of less than 1°. Many others are ROTO (Roll-Only Targeted Observations) images where the spacecraft rolled towards the east or west to take off-nadir images and the emission vector was thus close to the roughly east-west sun direction. Images from mid-phase E07 and onwards, however, were taken from

the “Relay-16” position in which the Mars Global Surveyor (MGS) spacecraft was rotated sixteen degrees off of nadir in a north-south direction. The approximations made in our calculation of the photometric angles will therefore be poorest for these Relay-16 images, but the errors in the brightness calculated for a given slope are still small in a fractional sense.

We use the incidence and emission angles for the image and rotate a hypothetical surface through a range of surface slopes, θ , to generate a suite of known μ^* and μ_0^* values for which the I^*/I ratio is then obtained. From these values, we create a lookup table that allows us to read off a value of θ quantized to the quarter degree for any value of I^*/I .

From *McEwen* (1991) the value of $L(\alpha)$ for most of the images in this study should vary from 0.45 to about 0.65. However, the simulations conducted with fractal topography, discussed below, show that the error resulting from the assumption of fixed L is minor, on the order of ten percent. We therefore estimate the value of $L(\alpha)$ for this study as 0.55.

For some images the emission angle was large, around 20°, which also contributed to a large phase angle, yielding a small value for L . These two effects can cause the I^*/I as a function of θ curve to become double-valued for high values of I^*/I and θ . However, given that these images are of terrain that is

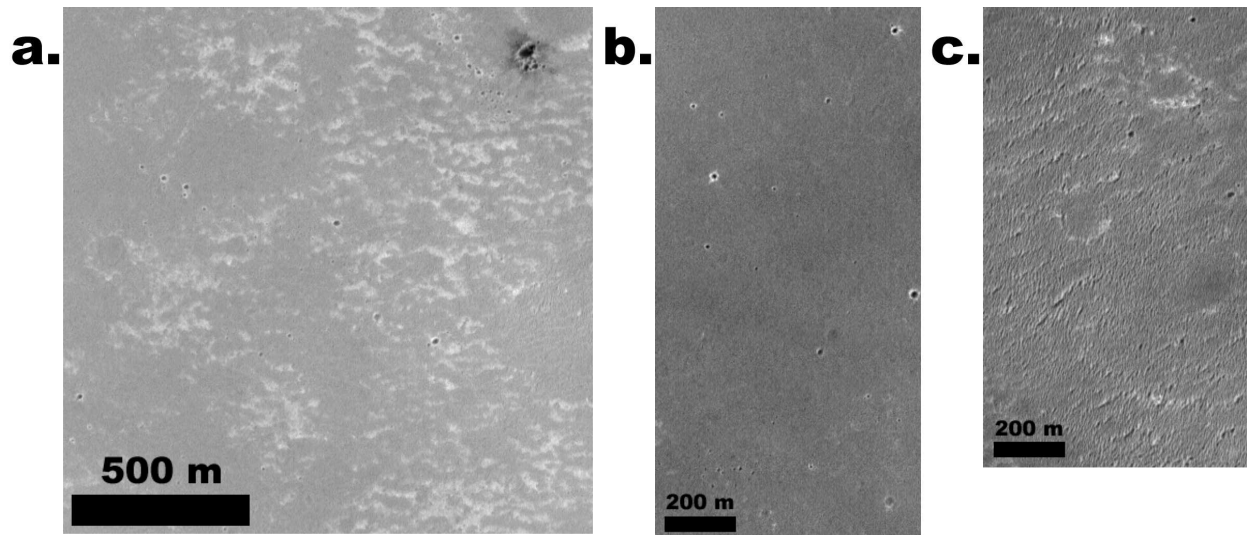


Figure 4: Portions of MOC image E03/01763 in Meridiani Planum. Figures *a*, *b*, and *c* are referred to as *Hematite 2a*, *Hematite 2b* and *Hematite 2c* by Kirk *et al.* (2003) and in Table 3.

flat at hundred-meter baselines, we seek the solution with the lower slope when this curve is multi-valued.

If (as is generally the case) there is little or no overall tilt to the image region chosen, then the average DN value of this region is a reasonable approximation to the DN of a level surface. We then use the ratio of each individual pixel’s DN to the average DN as our estimate of I^*/I , which can be compared with our lookup table to yield the value of θ that matches that brightness ratio.

2.3 Data Products

2.3.1 Slope Image

When we apply the above methods, we obtain a down-sun slope value for every pixel in each image that we measure. We effectively have a “slope image” where the value of each pixel is the slope in degrees of the corresponding original image pixel. These slope values can be placed into a greyscale image format such that positive slopes are brighter than 50% grey and negative slopes are darker, so that this slope image effectively becomes a shaded relief image that is independent of viewing angle and illumination angle, but not illumination azimuth. It is also instructive to create an absolute value version of this slope image (Figure 1c).

2.3.2 Slope Statistics

We compute the average slope and the root-mean-square (RMS) deviation for each image, as well as creating a plot of what percentage of the image is steeper than a given slope. This gives us an idea of the slope distribution at 6 meters/pixel.

2.3.3 RMS deviation with length scale

We can also continue to reduce the resolution of the images and perform our photoclinometry measurements on them again, as well as measure the slopes at the intrinsic resolution of the image. This allows us to build up information about how slopes change as a function of length scale. Following Shepard *et al.* (2001) we have degraded the resolution of the images to 10 m/pixel and 100 m/pixel. These resolution degradations (as well as the degradation to 6 m/pixel) are not achievable via integer summations of the original image pixels, instead a weighted average of the original pixel DN values is used to arrive at the desired degraded resolutions. We have found that the RMS slope deviations for an image at 6, 10, and 100 m/pixel fit the curve of RMS deviations versus length scale produced when we perform integer summing of the image. We use the 6 m/pixel values as a common resolution for the images in this study (there is no integer summable resolution that all images in the study could be degraded), and we

Viking 1 Landing Site Images

MOC Image Number	Resolution (m/pixel)	Incidence Angle (°)	Portion Measured
SP2/38303	4.97	66.74	all
M02/04443	1.497	39.63	all
M03/04873	1.492	43.16	all
M04/02209	1.496	46.93	all
M09/05589	1.497	54.87	all
M12/00448	1.608	49.52	all

Table 4: This table contains the MOC Image Numbers, their resolution in meters per pixel and their incidence angle in degrees, as well as an indication of how much of the image was measured.

provide the 10 and 100 m/pixel values for comparison with other roughness studies.

2.3.4 RMS Slope Image

In addition to these statistical measures of slope, we also create an “RMS slope image” (Figure 1d) that is useful for landing site evaluations. We take the slope image and perform a number of operations that yield an image whose pixels are values in degrees representing the RMS slope of meter-scale slopes within 100 m “footprints” on the image. We take the slope image and square the values. We then run a lowpass boxcar filter, 100 m on a side, through the squared image such that the resultant pixels $L(i, j) = S(i, j)/N(i, j)$. We then take the square root of the pixels in the boxcar filtered image, and sum that image down so that the resulting image has 100 m pixels. This is about the length scale that the airbag system will “see” from its first bounce to coming to a halt.

In the process of creating the various absolute value slope images, we found that the meter-scale slopes often changed when the underlying terrain changed morphology. This allowed us to use these slope images to help identify morphologic units, which are consistent with the morphologic units identified by others.

It is important to note that due to our automatic maximum haze estimate, the slopes that we report in this study are upper bounds to the down-sun slope values, not the true slope values.

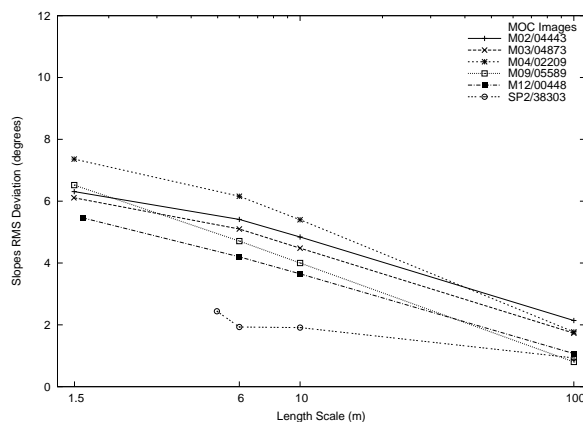


Figure 5: Viking 1 Landing Site RMS Roughness. This figure shows the RMS slope deviation in degrees calculated from the slopes in each of the images listed. Slopes statistics are obtained at longer length scales by reducing the resolution in the images, and performing the photogrammetry technique on those reduced resolution images.

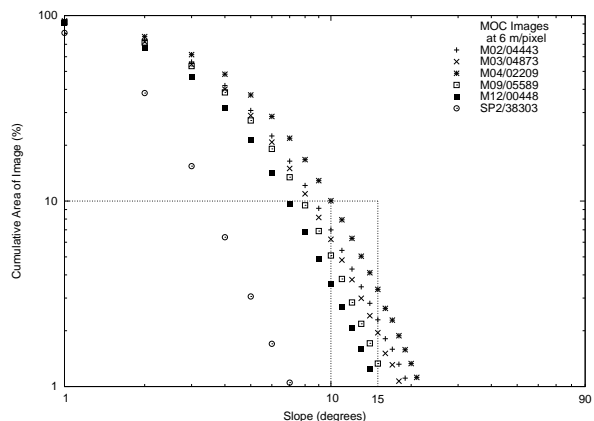


Figure 6: Viking 1 Landing Site Slope Distribution. This figure plots what percentage of an image has slopes steeper than some value. The dashed lines are guides to show where only ten percent of an image is steeper than 10° and 15° respectively. Since all the curves for images in the Viking 1 landing site pass within the box defined by the 15° guides, then all the images have less than 10% of their slopes which are steeper than 15° . In addition to the plot of RMS roughness, this kind of plot gives an idea of the distribution of steep slopes in each image.

Viking 2 Landing Site Images

MOC Image Number	Resolution (m/pixel)	Incidence Angle ($^{\circ}$)	Portion Measured
M02/01764	1.569	47.81	all
M03/07241	1.565	58.93	all
M09/02236	3.136	75.13	all
M11/01288	4.7	75.10	all
M12/00485	1.569	72.04	all
M13/00163	6.265	67.80	all

Table 5: This table contains the MOC Image Numbers of all the images in the Viking 2 Landing site area for this study.

3 Calibration

3.1 Synthetic Fractal Topography

It is of interest to assess the accuracy of our point photogrammetry method by applying it to cases in which the slope statistics are known or can be estimated independently. One way to do this is to simulate images from known digital elevation model (DEM) data, which allows us to control the illumination geometry and the presence or absence of albedo variations and haze. Random self-affine fractal surface models (*Turcotte, 1997*) are especially convenient in that they are easy to generate and contain roughness that varies with horizontal scale in a way that crudely mimics natural surfaces. A series of such fractal models 1025 elevation posts on a side (in order to simulate images with 1024 pixels on a side) were generated and used both for this study and that of the behavior of two-dimensional photogrammetry by *Kirk et al. (2003)*. The Fourier-domain algorithm of *Turcotte (1997)* was not used; instead we constructed the terrains by interpolating white noise components to scales increasing by successive factors of two, scaling their variances to produce the desired value of the Hurst exponent, H , and adding them. The Hurst exponent, H , or Hausdorff parameter, governs the variation of roughness with baseline (e.g. *Shepard et al., 2001; Turcotte, 1997*). We verified that the value of H that results was equal to the intended value to high accuracy by using the Fourier analysis techniques discussed for slope versus baseline analysis by *Kirk et al. (2003)*.

As shown in Table 1, these models differed in their RMS slope on a pixel-center-to-pixel-center baseline and also in their value of H . Models with $H = 0.8$ are most similar to the candidate landing

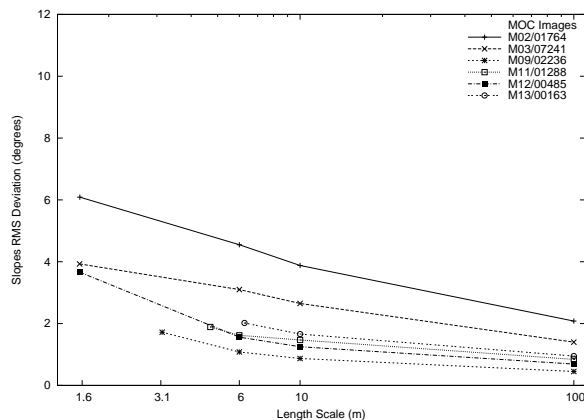


Figure 7: Viking 2 Landing Site RMS Roughness.

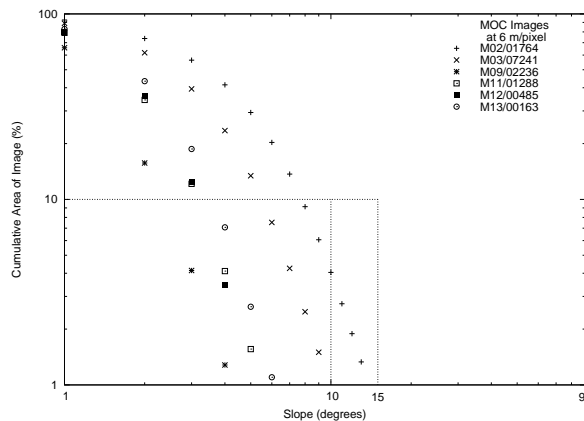


Figure 8: Viking 2 Landing Site Slope Distribution.

sites (*Kirk et al., 2003*); smaller H corresponds to a greater preponderance of short-baseline roughness. Models based on the $H = 0.8$ fractal but highpass or lowpass filtered to exclude roughness at scales larger or smaller than 16 pixels were also examined. The majority of cases were scaled to have bidirectional RMS slopes (measured between pixel centers as discussed below) of 1° but cases with 10° slopes were also investigated.

Images of the fractal surface models were simulated with incidence and emission angles of 45° and 0° respectively (typical of the MOC images used in this study) and illumination azimuths both on the sample axis and 22.5° oblique to it. Images were generated both with the $L = 0.55$ lunar-Lambert model used in our point photogrammetry analyses, and with a *Minnaert (1941)* photometric function with $k = 0.72$, appropriate to the martian surface

Pathfinder Landing Site Images

MOC Image Number	Resolution (m/pixel)	Incidence Angle ($^{\circ}$)	Portion Measured
SP1/23703	2.549	48.83	all except for the 1.3 km diameter crater
M08/01772	1.488	50.62	all
M10/00740	1.489	52.05	all
M10/03058	1.567	51.56	all
M11/01311	1.497	49.27	all
M11/02414	1.575	47.92	all except for the 1.5 km diameter crater

Table 6: This table contains the MOC Image Numbers of all the images in the Pathfinder Landing site area for this study.

with a 45° phase angle (*Kirk et al.*, 2000). The difference between the results when these two models are used to synthesize the images gives some idea of the errors caused by our choice of constant $L = 0.55$. Uniform photometric properties were implicit in the generation of the synthetic images (*Kirk et al.*, 2003, Figure 7). To test the effects of spatial albedo variations, a separate bandpass-filtered fractal albedo map was generated and applied multiplicatively to a subset of images (*Kirk et al.*, 2003, Figure 8).

Table 1 shows the results for uniform albedo, comparing bidirectional RMS slopes measured directly from the synthetic DEMs to those recovered by point photogrammetry. For each case, two direct measurements are shown, differing in how the fractal DEM data are interpolated in order to calculate slopes. Excellent agreement ($\sim 0.5 - 1\%$ relative error in RMS slope for all but the roughest cases) is obtained between photogrammetry and direct measurements of the slope across the center of each pixel, from the midpoint of one edge to the midpoint of the opposite edge. Not surprisingly, this is equivalent to the average slope over the whole pixel, which enters into the pixel brightness and is then interpreted by photogrammetry. Slopes measured from the center of a pixel to the center of the adjacent pixel are smoother as a natural consequence of the roughness of the fractal surface model at small scales, including across individual pixels. The distinction matters for comparison of our results with those from area photogrammetry (e.g. *Kirk et al.*, 2003). Although this technique produces height estimates at pixel corners, these are usually interpolated to pixel

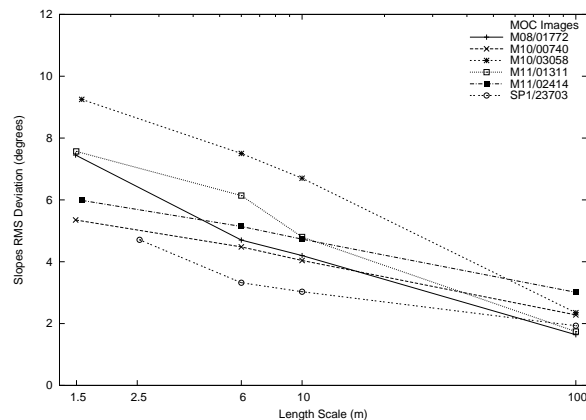


Figure 9: Pathfinder Landing Site RMS Roughness.

centers (in order to provide a DEM that has the same dimensions as the input image). Slope statistics calculated from these pixel-center heights will tend to be slightly smoother than statistics from point photogrammetry. The magnitude of the effect depends on the roughness of the surface at the single-pixel scale, e.g. on H . If the surface is smooth at this scale, as for our lowpass-filtered case and surfaces in real images (which are smoothed slightly by the point-spread function of the camera) then the difference between bidirectional slopes calculated by point and area photogrammetry is much smaller than for a strictly fractal surface.

When the roughness of the surface is increased to 10° (pixel center-to-center; this is rougher than all but a few candidate sites described below), point photogrammetry underestimates the bidirectional RMS slope by a little more than 2%. As discussed above, our assumption that slopes lie in the plane of the sun (where they have the maximum effect on image contrast) is responsible for this small underestimation. Table 1 also shows that using our lunar-Lambert photometric model to interpret images formed with a different (but equally Mars-like) Minnaert model results in a roughly 5% error in the bidirectional slope estimates. In the cases shown here, our photometric model causes the slopes to be underestimated. For images of the real surface of Mars, whose photometric behavior varies somewhat with phase angle, we anticipate that slopes will be sometimes overestimated, sometimes underestimated, but are unlikely to be in error by more than a few percent of the actual bidirectional slope value because of this effect. Finally, we note that

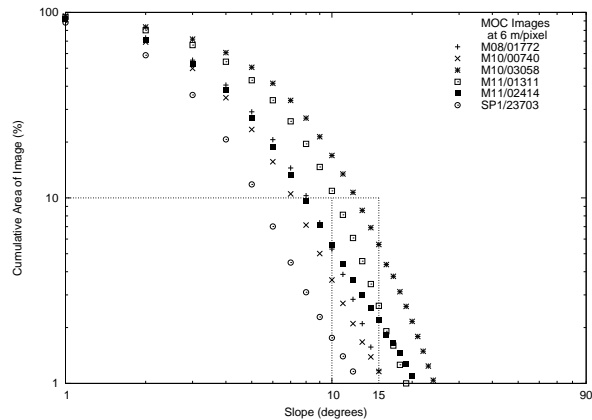


Figure 10: Pathfinder Landing Site Slope Distribution.

similar results were obtained for illumination along the sample axis and at 22.5° (a typical solar azimuth for the MOC images), as well as at other azimuths not shown in Table 1.

Table 2 shows results when spatially nonuniform albedo is introduced into the images. A RMS albedo variation of 0.63% of the mean was selected for the test; this is the amount of brightness variation that would also result from a slope of 0.5° . The increase in inferred bidirectional RMS slope, from 1.31° to 1.41° is precisely what is expected in our simulation: because the true roughness and albedo-related “slopes” are independent, their variances add, giving a total bidirectional RMS slope estimate of $\sqrt{1.31^2 + 0.5^2} = 1.41$. In reality, albedo variations may not always be independent of roughness. Albedo changes can correspond to compositional changes, and different geologic materials can have different roughness properties.

Although the amplitude (and spatial distribution) of albedo variations in a given real image will certainly differ from that assumed in this simulation, if this amplitude can be estimated then a similar calculation can be used to estimate the apparent roughening that will result. The magnitude of this albedo-induced apparent slope is independent of sun direction, because point photogrammetry always gives the slope in the sun direction rather than in a fixed direction. For area photogrammetry, in contrast, the albedo-induced roughening is much greater when the sun crosses the slope baseline (e.g., the sample axis) at an angle. However, digital filtering of the DEM to suppress the artifacts due to albedo

Athabasca Valles Landing Site Images

MOC Image Number	Resolution (m/pixel)	Incidence Angle ($^\circ$)	Portion Measured
M02/00581	5.875	37.75	central
M04/02002	5.867	42.10	all
M07/00614	5.873	43.26	southern
M07/01888	5.874	43.80	central
M09/00662	2.934	45.52	all
M09/02518	5.864	45.30	northern
M11/00331	2.926	41.81	all
M12/01114	5.864	35.97	all
M12/02516	6.074	25.35	all
M18/01080	5.872	26.21	southern
E10/01384	3.1	43.67	southern
E10/02604	6.18	42.23	northern
E10/03841	3.09	41.56	northern
E11/00142	3.09	40.68	all
E11/02913	3.1	38.37	all
E11/03799	3.1	37.24	all
E12/00071	3.1	36.04	all
E12/01728	1.75	35.01	all
E12/01946	4.64	33.5	all
E12/02746	4.63	31.53	northern
E12/02967	4.16	29.53	all
E13/00030	3.09	30.73	all
E13/00697	3.09	29.5	all
E13/01475	1.65	26.73	all
E13/02142	4.65	27.15	all

Table 7: This table contains the MOC Image Numbers of all the images in the Athabasca Valles Landing site area for this study.

variations yields slope errors that are comparable to those for point photogrammetry regardless of the solar azimuth (*Kirk et al.*, 2003).

3.2 Comparison to Area Photogrammetry

It is also of interest to compare slope estimates from our point photogrammetry with an independently developed method in cases based on real images of Mars. For such comparisons, we are of course not privy to the “true” slope distributions but can determine whether our results are consistent with other methods. In particular, we compared our results with those obtained by *Kirk et al.* (2003) from the same images by using area photogrammetry. It is useful to do such comparisons in several ways. By

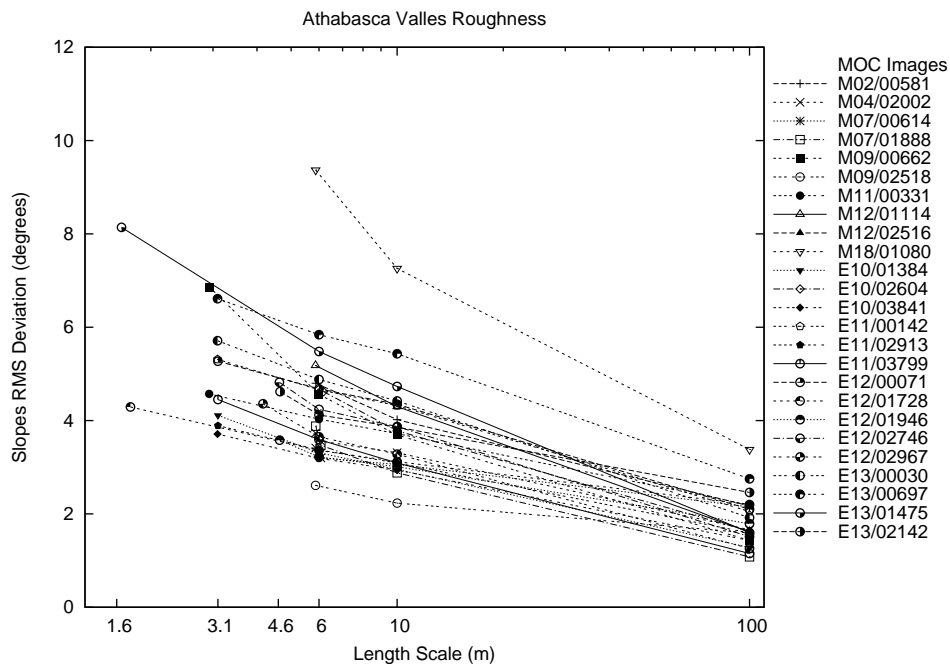


Figure 11: Athabasca Valles Site RMS Roughness.

choosing an image in which albedo variations are minimal and using a relatively precise haze estimate obtained by comparing the image to a stereo DEM of the area (*Kirk et al.*, 2003) we can establish whether point and area photogrammetry are as consistent for real martian topography as they are for synthetic, fractal surfaces. By relying instead on our darkest-pixel estimate for the haze we can quantify the effect this has on the accuracy of slopes. Finally, by looking at other areas with more extreme albedo variations, we can say something about the relative sensitivity of the two methods to such effects.

The area photogrammetry technique has a number of advantages over our point photogrammetry. It allows for the effect of cross-sun slopes on brightness, rather than assuming all brightness variation comes from slopes up- or down-sun, which is true to first order but not precisely true. Area photogrammetry allows the modeling of slopes cross-sun as well as down-sun, and hence allows determination of adirectional slopes and slopes in particular baselines not tied to the Sun. The cross-sun slopes will always be more weakly determined than those down-sun since they have only a second order effect on brightness and most of the cross-sun information

comes from continuity of the surface.

The area photogrammetry method also suffers from the problems of haze and albedo, but in some ways they are easier to handle. The elevation model produced by the area method can be compared with an a priori DEM from stereo or altimetry in order to calibrate the haze by requiring that the heights of resolved features agree. Area photogrammetry assumes a constant albedo surface and is not immune to albedo-related artifacts. However, the DEM that is generated makes albedo artifacts very apparent as nonsensical topographic “stripes”. Finding these “stripes” is an excellent quality check, and makes it possible to reduce such artifacts by tailored filtering. In this process, stripes are isolated from other topography by first filtering the DEM with a lowpass filter along their length and then with a highpass filter across their narrowest extent. The estimated stripe component can then be subtracted from the original DEM. This filtering process must in general be done several times, each step removing stripes in a particular size range. Filtering reduces the erroneous contribution to slopes in the stripe (down-sun) direction, and even more dramatically reduces the much greater errors in slopes along baselines that

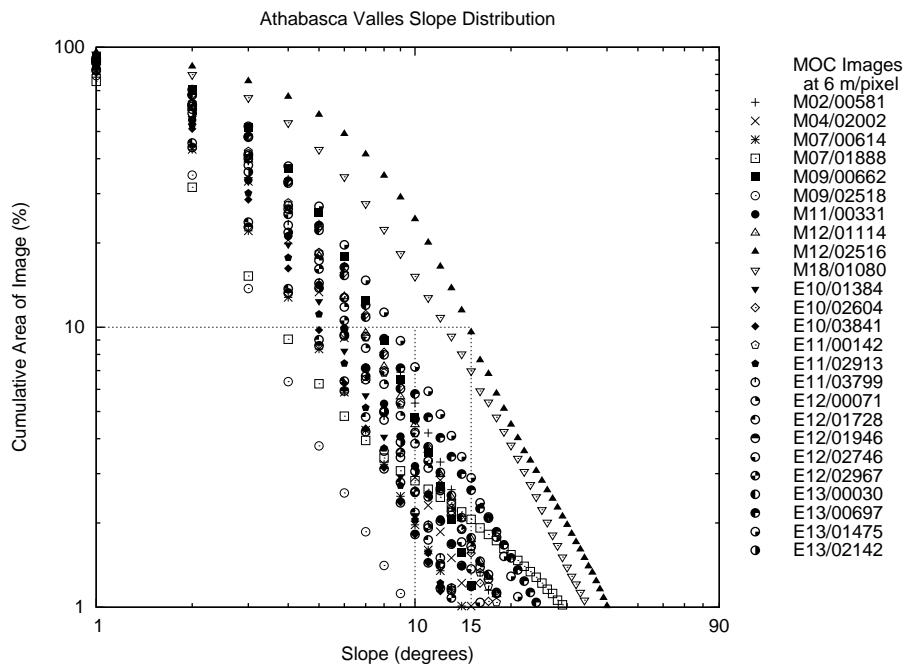


Figure 12: Athabasca Valles Site Slope Distribution.

cut across the stripes.

Two portions of the MOC image E02/00665, which is in the Gusev Crater landing ellipse, were measured with both techniques. *Kirk et al. (2003)* refer to the portion of smooth cratered plains in Thira Crater as *Gusev 1d* (Figure 2), and the knobby etched plains south of Thira Crater as *Gusev 1e* (Figure 3), as do we.

Table 3 shows that area and point photogrammetry with the same haze estimates yield essentially identical bidirectional slope estimates for the smoother region, *Gusev 1d*, while the point photogrammetry bidirectional slope for the rougher region, *Gusev 1e*, is about 5% lower than that from the area method. The tendency of point photogrammetry to underestimate steeper slopes is well understood as discussed above, and this result is generally consistent with our fractal simulations shown in Table 1. Given the $\leq 5\%$ slope errors that may be introduced by our choice of photometric model, the agreement between results for Gusev is surprisingly good given the same haze estimate.

When we use the darkest or minimum pixel value in the scene as the haze estimate, our point photogrammetry method yields different results. Comparing

these results for the Gusev image regions to those using the *Kirk et al. (2003)* haze estimation indicates how the bidirectional RMS slope values in this study for the landing ellipses are, in general, providing an upper limit to the slopes. In the case of *Gusev 1e*, the darkest pixel haze estimate and the *Kirk et al. (2003)* haze estimate are similar, yielding bidirectional RMS slopes that are similar. However, in *Gusev 1d*, the darkest pixel haze is much greater than the *Kirk et al. (2003)* haze, and the resultant bidirectional RMS slope is much greater as well. These portions of the E02/00665 image in Gusev Crater are representative of the best case for our technique. There appear to be no albedo variations complicating the surface, and so the major contribution to error is the haze. It is also representative in that the haze estimate from the darkest pixel either does a good job of estimating the haze, or overestimates it, yielding upper limits to the bidirectional RMS slopes.

The difference in haze estimates and RMS slopes from photogrammetry illustrates the relationship between the slope error and the haze. The RMS slope is going to be inversely proportional to the difference between the average (flat) DN and the assumed haze

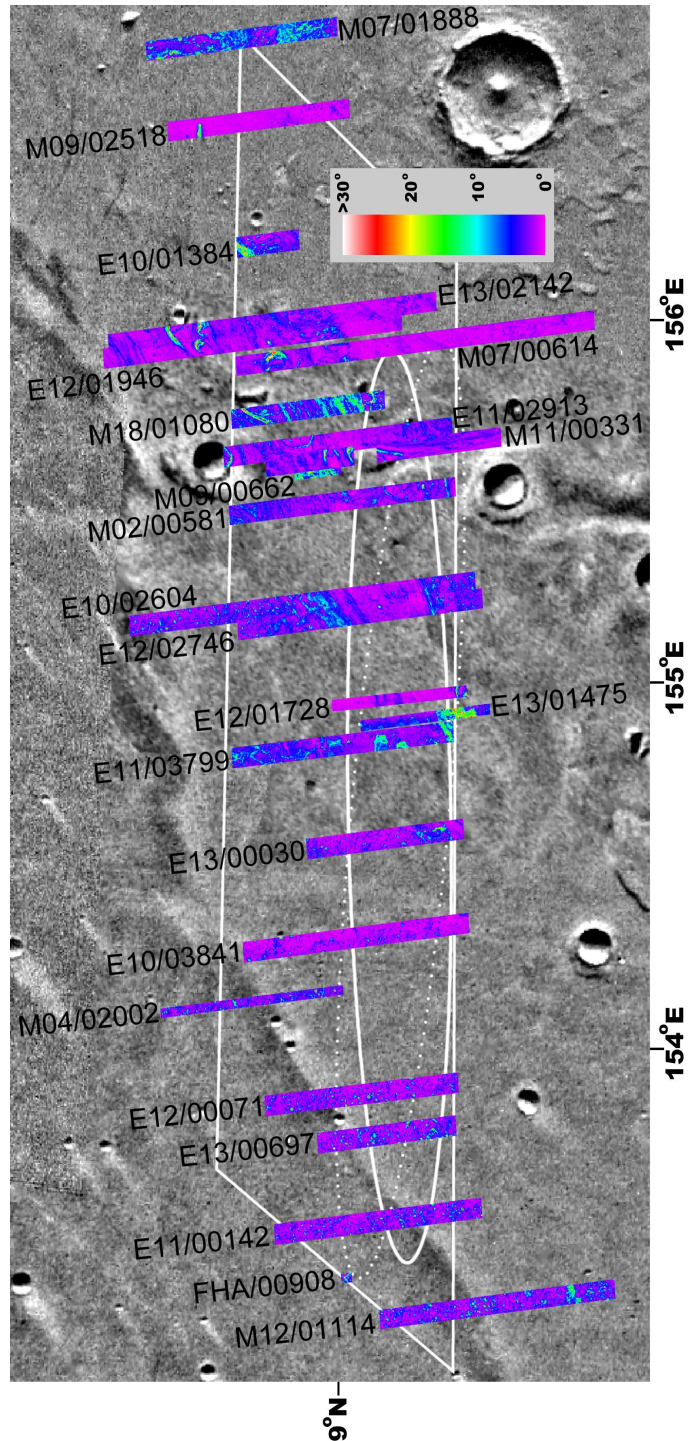


Figure 13: Athabasca Valles RMS Slope Image Mosaic. The colored RMS slope images of the various MOC images in this area are mosaicked onto a basemap of Viking Orbiter images (MDIM 2). In the case of Athabasca Valles, more than just the terrain of one ellipse was requested for more complete MOC coverage, and the rhombus indicates that high-coverage area.

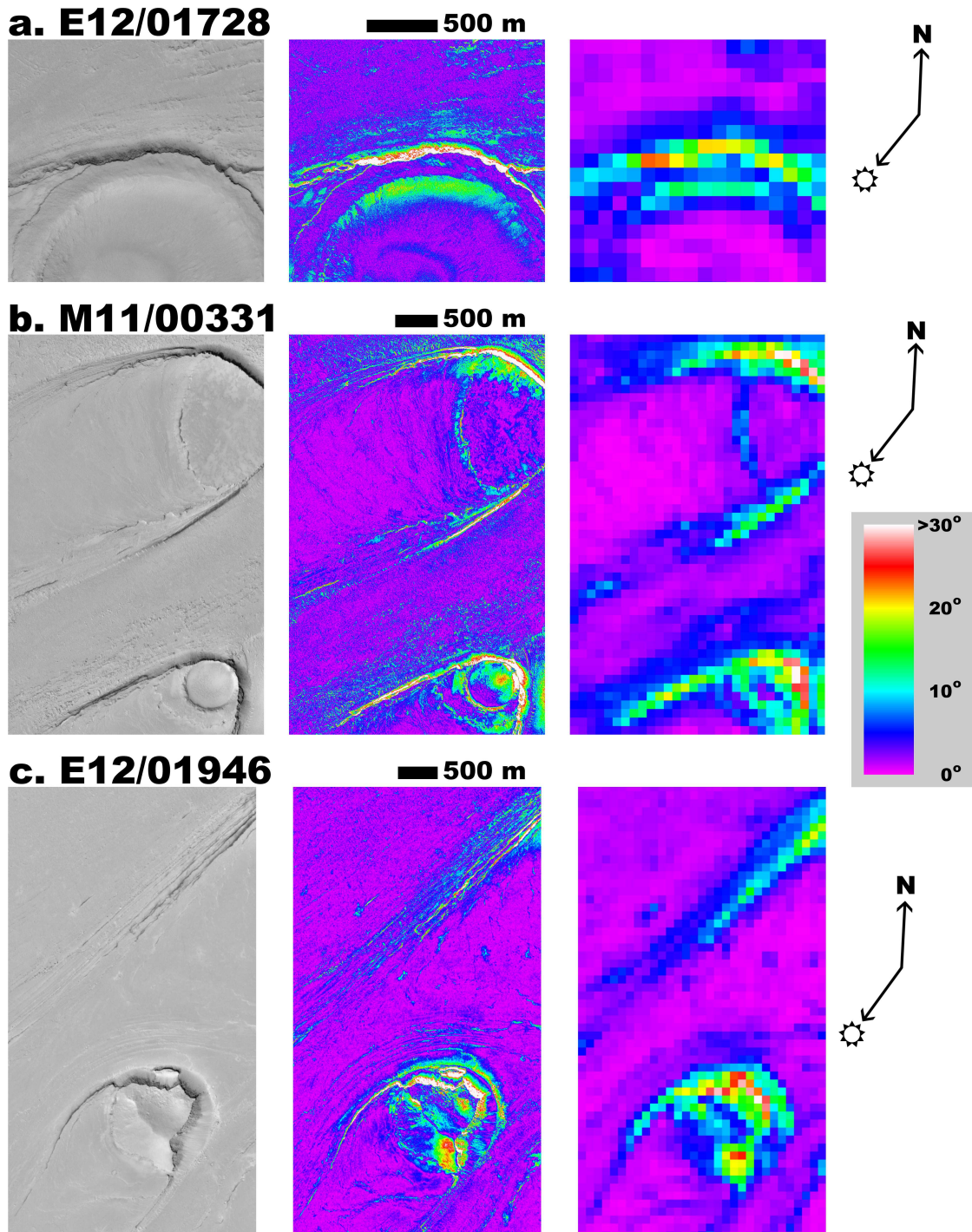


Figure 14: Each of these three figures contain a portion of a cleaned and calibrated MOC image in the Athabasca Valles study area, a slope image at the original resolution of the MOC image, and an RMS slope image. The large pixels in the RMS slope image are 100 m across. (a) Portion of E12/01728. This image shows a crater whose northern flank has been eroded. (b) Portion of M11/00331. This image shows some of the fluviably modified mesas in Athabasca Valles. (c) Portion of E12/01946. This image also shows some of the fluviably modified forms in Athabasca Valles.

Elysium Planitia Landing Site Images

MOC Image Number	Resolution (m/pixel)	Incidence Angle ($^{\circ}$)	Portion Measured
E17/01505	3.10	25.58	all
E18/00019	3.10	26.23	all
E18/00429	3.10	26.90	all
E18/00898	3.10	27.60	all
E18/01327	3.10	28.31	all
E18/01455	4.17	24.77	all

Table 8: This table contains the MOC Image Numbers of all the images in the Elysium Planitia Landing site area for this study.

DN (i.e., raising the haze estimate increases the apparent slope).

Also in Table 3 are measurements of E03/01763 in the Meridiani Planum landing site. These image portions (Figures 4a, 4b, and 4c) show how albedo variations will affect photoclinometric measurements. We know that the terrain in these images are relatively smooth plains, and so the shading contrasts are from albedo variations. Still, both the area photoclinometry of *Kirk et al.* (2003) and the point photoclinometry of this study yield similar results. This is with the resultant DEMs from area photoclinometry destriped to minimize albedo effects. Without these corrections, the bidirectional RMS slopes from area photoclinometry are greater.

However, when we use the darkest pixel haze estimate for point photoclinometry in these regions of E03/01763, we get a high value, and the bidirectional RMS slopes reported are significantly greater than those reported when a more reasonable haze estimate is used. This again illustrates how haze is the biggest source of error, but that albedo variations can magnify that error.

The results of both area and point photoclinometry when the *Kirk et al.* (2003) haze estimates are used compare reasonably well to *Kirk et al.* (2003) stereo estimates of slope in a few other areas of the ellipse. These were $\sim 1.5 - 2.5^{\circ}$ but contained estimated errors of $1 - 1.5^{\circ}$ indicating the slopes are very low and hard to measure in this region.

Thus the slope estimates from photoclinometry of either type are clearly heavily influenced by albedo variations and are likely to be severe overestimates. One can look at Figure 4a and 4b and see that Figure 4a is probably not any rougher in reality than Figure 4b, it merely has more albedo

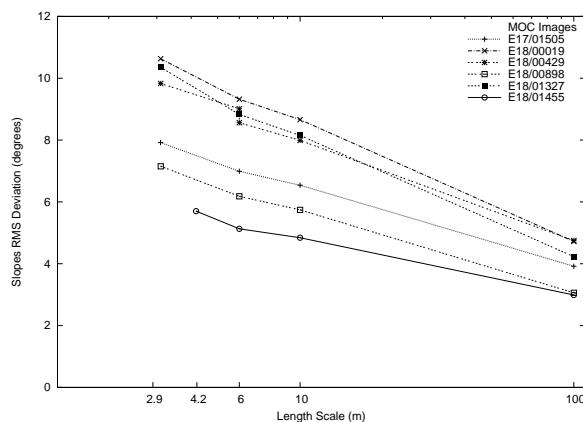


Figure 15: Elysium Planitia Site RMS Roughness.

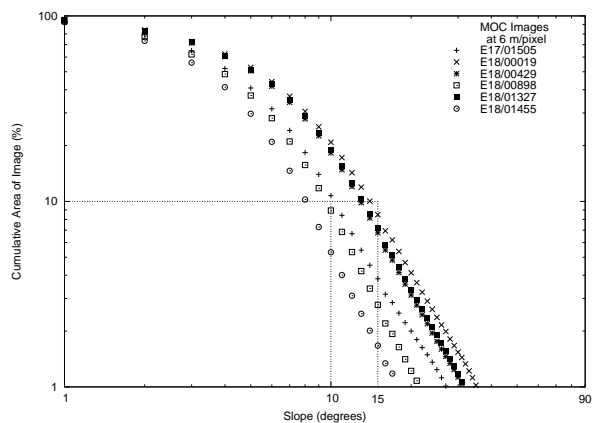


Figure 16: Elysium Planitia Site Slope Distribution.

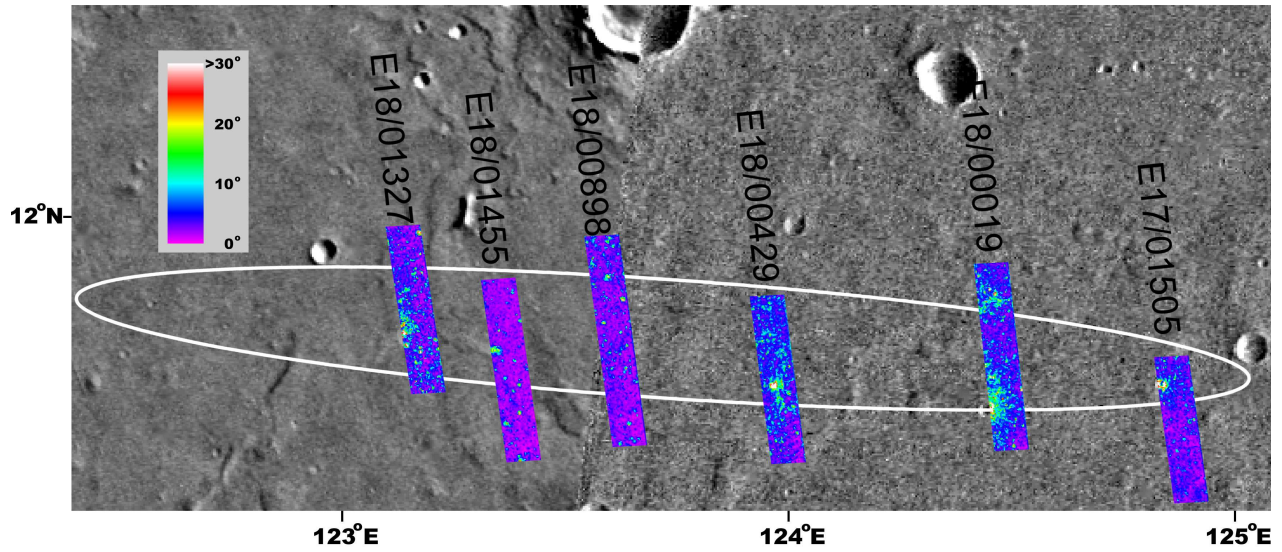
variation. Nevertheless, even these “contaminated” slope estimates are very smooth, so the conclusions about the safety of the Meridiani Planum site (that are discussed below in §4.7) are secure.

The advantage of our point photoclinometry method over the area photoclinometry method in this type of study is that it is easier and faster to apply to entire images, giving much better areal coverage.

3.3 Comparison to Previous Landing Sites

In order to gain another estimate for the precision of our technique, we decided to apply it to MOC images taken of the regions around the Viking 1, Viking 2, and Pathfinder landing sites. This allowed us to make good use of the only known areas of “ground

a.



b.

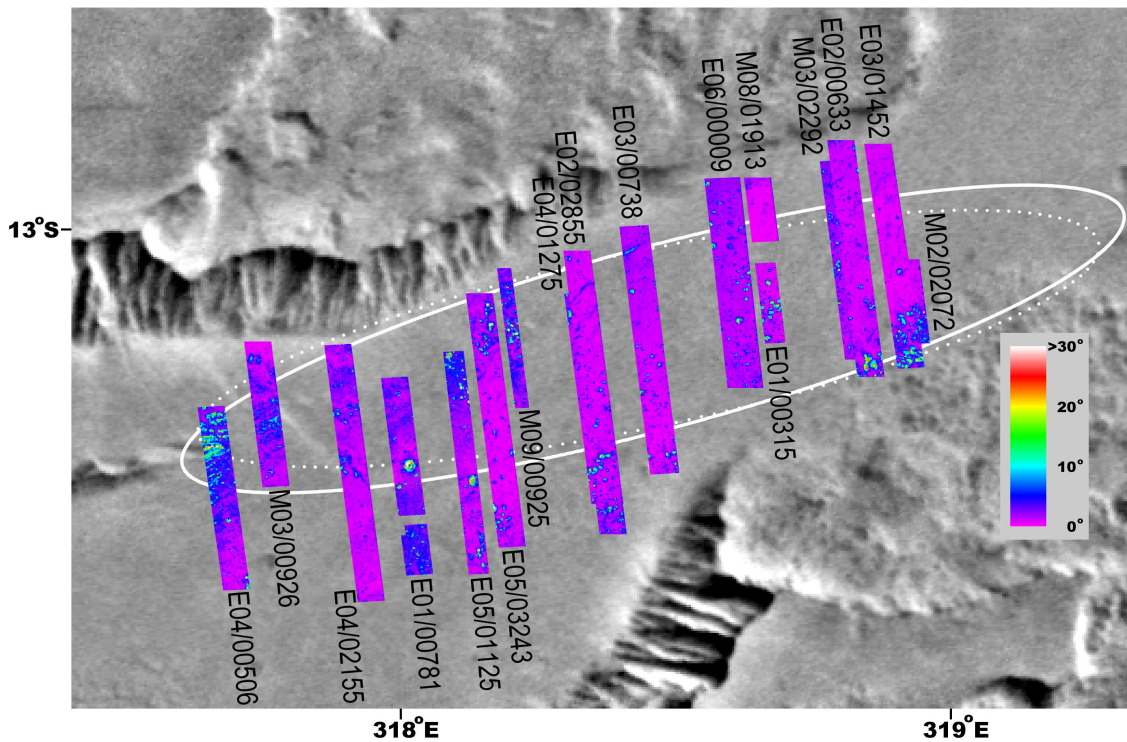


Figure 17: (a) Elysium Planitia RMS Slope Image Mosaic. (b) Eos Chasma RMS Slope Image Mosaic. The solid ellipse is the location of the landing ellipse at the opening of the launch window, and the dotted ellipse is the location at the close of the launch window. In both of these images the colored RMS slope images of the various MOC images in this area are mosaicked onto a basemap of Viking Orbiter images (MDIM 2).

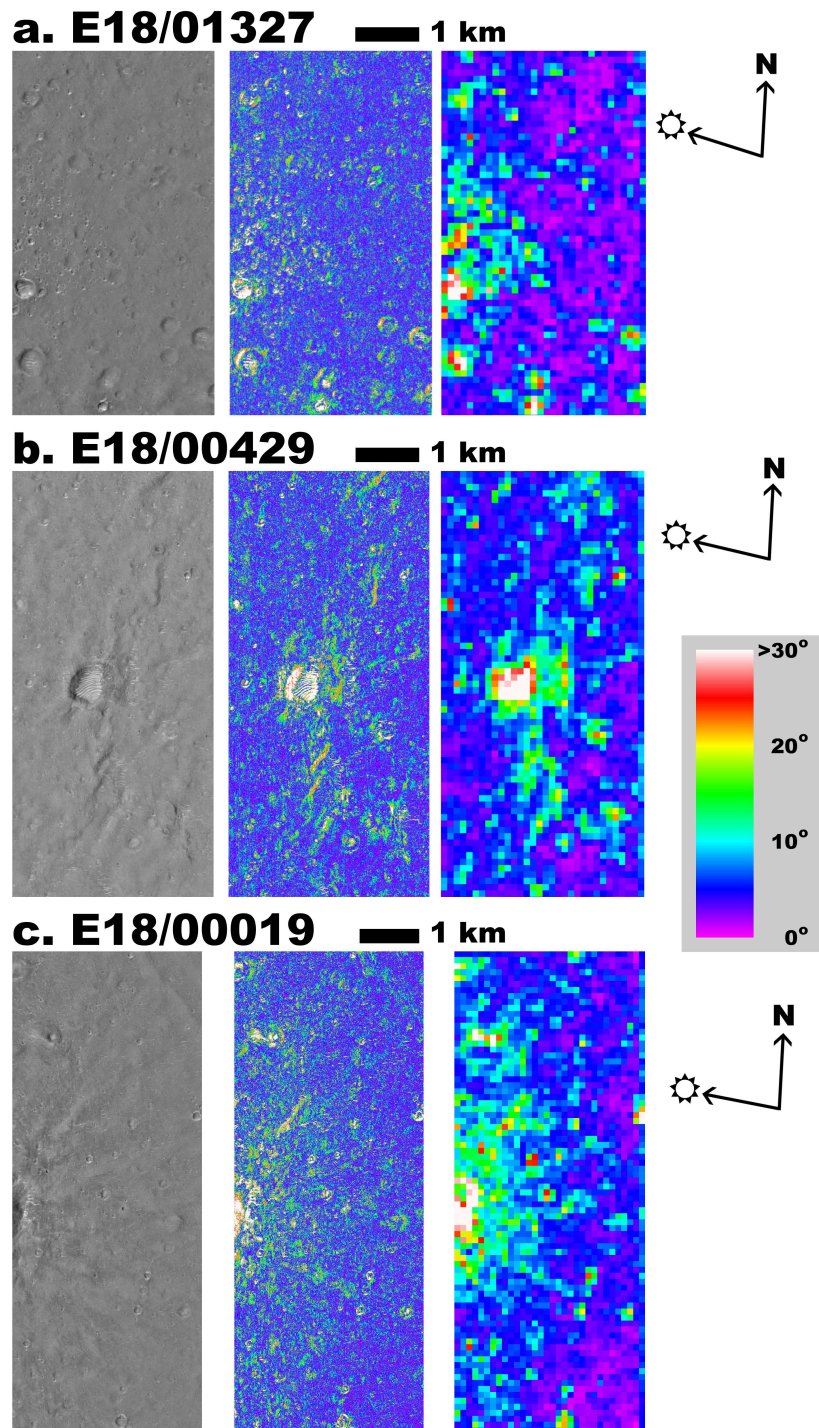


Figure 18: Each of these three figures contain a portion of a cleaned and calibrated MOC image in the Elysium Planitia study area, a slope image at the original resolution of the MOC image, and an RMS slope image. The large pixels in the RMS slope image are 100 m across. (a) Portion of E18/01327. This image shows how a pattern of small fresh craters are easily seen in the slope images. (b) Portion of E18/00429. This image displays the slopes on a ridge running south of a crater. (c) Portion of E18/00019. The easternmost rim of a crater and the steeper slopes on its ejecta are picked out in the slope images here.

Eos Chasma Landing Site Images

MOC Image Number	Resolution (m/pixel)	Incidence Angle (°)	Portion Measured
M02/02072	5.676	45.96	northern
M03/00926	5.681	44.51	southern
M03/02292	5.68	43.97	northern
M08/01913	5.682	37.77	southern
M09/00925	2.841	35.19	southern
E01/00315	2.84	51.03	all
E01/00781	2.85	51.05	all
E02/00633	2.87	49.55	central
E02/02855	4.3	48.25	central
E03/00738	3.06	49.0	all
E03/01452	2.86	46.95	southern
E04/00506	2.85	45.53	all
E04/01275	3.3	47.04	northern
E04/02155	2.87	44.28	southern
E05/01125	2.87	43.13	all
E05/03243	2.85	41.99	southern
E06/00009	3.67	38.78	northern

Table 9: This table contains the MOC Image Numbers of all the images in the Eos Chasma Landing site area for this study.

truth” on Mars as a benchmark for our technique before we attempted to apply it to the landing ellipses for the MER 2003 mission.

3.3.1 Viking 1

Table 4 shows the MOC images that were near the location of the Viking 1 landing site (*Morris and Jones, 1980; Zeidler and Oberst, 1999; Parker et al., 1999; Parker and Kirk, 1999*). On the basis of the information from the Viking 1 lander’s leg stroke gauges and camera measurements of the horizon, the local surface slope from one footpad to another (about 2.5 m) is about 1° (*Shorthill et al., 1976a*). *Binder et al. (1977)* indicate a more general slope to the area of 1.5° towards the northwest. The lander stereo-derived topographic map of *Binder et al. (1977, figure 5)*, indicates that the steepest slopes that can be found are about 10°, with most slopes less than that.

Our measurements in Figures 5 and 6 show the relative smoothness of the Viking 1 landing site images. The maximum estimate of bidirectional RMS slopes in the images that we measured was $\sim 6^\circ$ on length scales of 1.5 m. Additionally, $\sim 90\%$ of the 6 m length scale slopes in these images are less than

10°.

3.3.2 Viking 2

Near the proposed location of the Viking 2 lander (*Parker and Kirk, 1999; Oberst et al., 2000*), we measured the images listed in Table 5. The Viking 2 landing site is very flat and has less than 1 m of relief to a radial distance of 100 m from the lander (*Mutch et al., 1977*). However, based on lander leg stroke, guidance system information, and horizon measurements the lander itself is at a 6° tilt (*Shorthill et al., 1976b*). It is thought that one of the footpads is either perched on a rock or in a depression.

The statistics in Figures 7 and 8 show how our technique reports lower maximum bidirectional RMS slopes for the Viking 2 landing area than for the Viking 1 area. Our estimate of the maximum bidirectional RMS slopes at the shortest length scales is about 4°, and at length scales of 6 m, more than 90% of the slopes in these images are less than 10°.

3.3.3 Pathfinder

The images in Table 6 were close to or overlapping the Pathfinder landing site (*Parker and Kirk, 1999*). Stereo images from the Imager for Mars Pathfinder (IMP) were used to determine the topography in the inner area around the lander, and it was determined that the RMS slope value was $\sim 4^\circ$ (*Kirk et al., 1999; Ward et al., 1999; Golombek et al., 1999; Smith et al., 1997, plate 4*).

Our measurements of these MOC images are in Figures 9 and 10. Our estimation of the maximum bidirectional RMS slopes at the smallest length scales is $\sim 7^\circ$, and almost all of the slopes in these images are less than 15° and most are less than 10°.

Our results for the Viking 1, Viking 2, and Pathfinder landing sites show those regions to be smooth at the meter scale. This is reassuring due to the meter-scale smoothness observed by the landers themselves. For the only three locales on the Martian surface for which we have ground truth, our technique appeared to report accurate upper limits to the slopes observed by the landers.

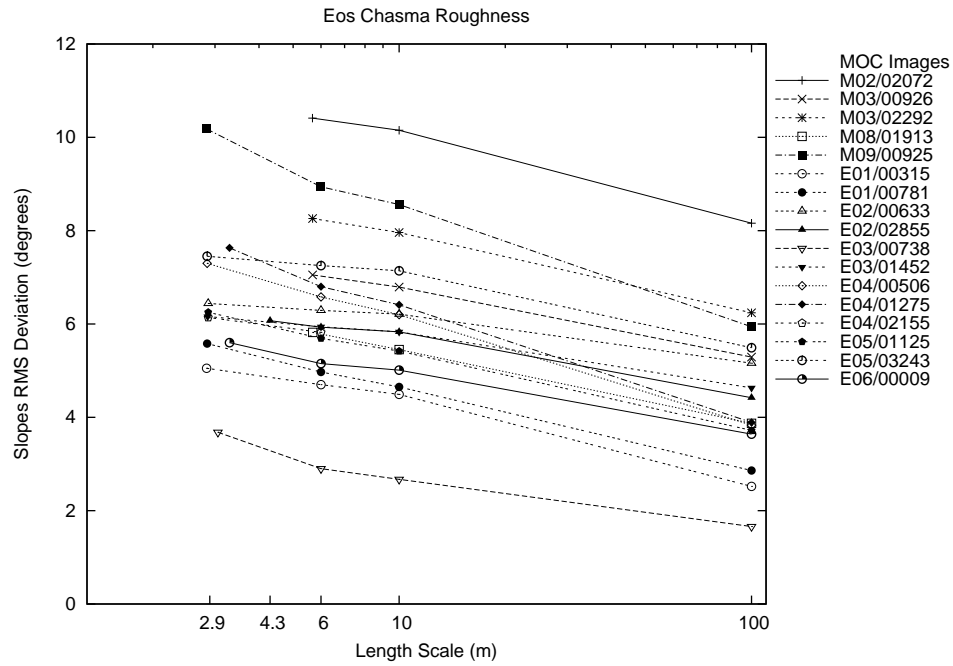


Figure 19: Eos Chasma Site RMS Roughness.

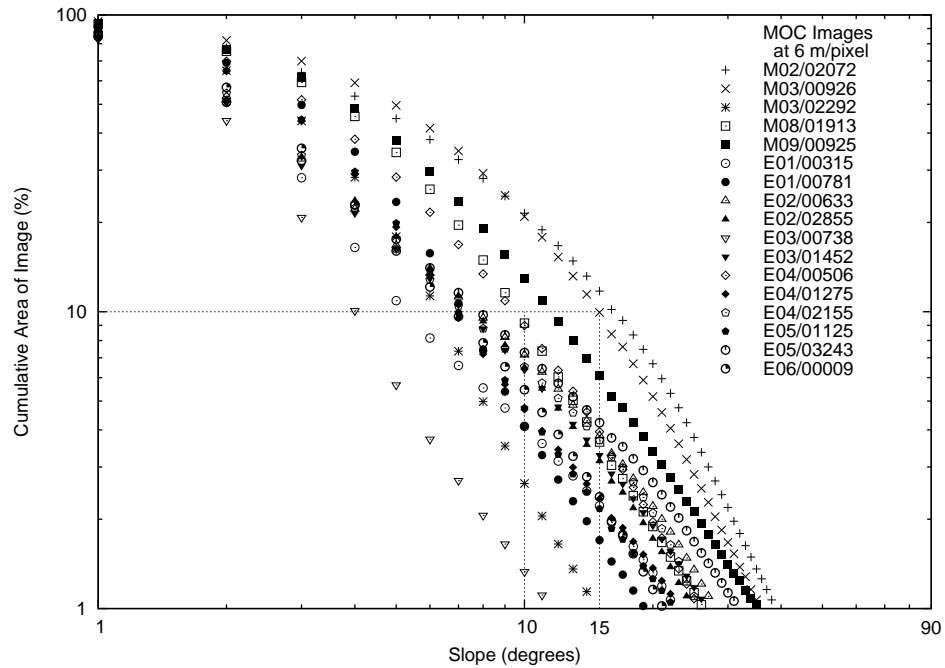


Figure 20: Eos Chasma Site Slope Distribution.

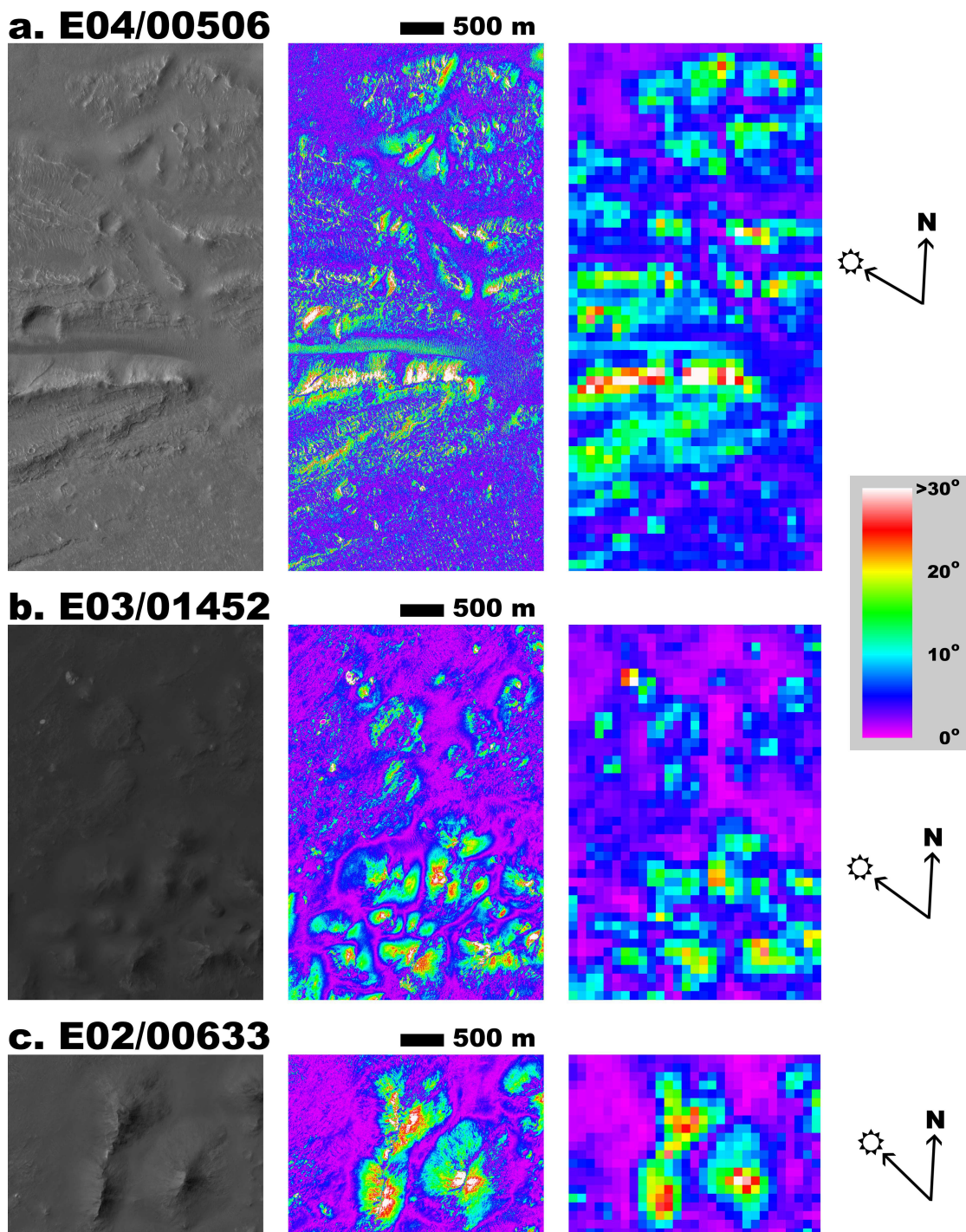


Figure 21: Each of these three figures contain a portion of a cleaned and calibrated MOC image in the Eos Chasma study area, a slope image at the original resolution of the MOC image, and an RMS slope image. The large pixels in the RMS slope image are 100 m across. (a) Portion of E04/00506. This image shows the streamlined landform on the western edge of the ellipse. (b) Portion of E03/01452. Hummocky terrain in the southeast portion of the ellipse can be seen. (c) Portion of E02/00633. More of the hummocky terrain in the southeast portion of the ellipse can be seen in this image portion.

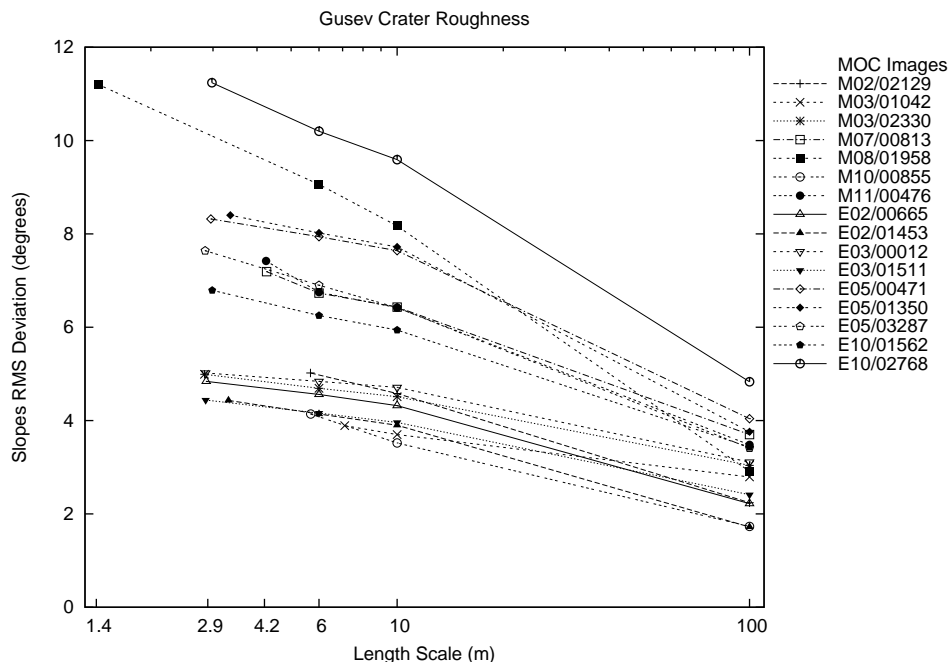


Figure 22: Gusev Crater Site RMS Roughness.

Gusev Crater Landing Site Images

MOC Image Number	Resolution (m/pixel)	Incidence Angle (°)	Portion Measured
M02/02129	5.674	46.63	all
M03/02330	2.839	44.43	southern
M07/00813	4.259	40.38	northern
M08/01958	1.419	37.48	northern
M10/00855	5.683	30.55	northern
M11/00476	4.246	26.43	northern except NW corner
E02/00665	2.87	50.72	northern
E02/01453	3.32	48.33	northern
E03/00012	2.86	49.31	northern
E03/01511	2.86	47.97	central
E05/00471	2.96	43.25	northern
E05/01350	3.36	41.05	all
E05/03287	2.85	42.3	northern
E10/01562	2.98	28.42	all
E10/02768	2.98	27.40	all

Table 10: This table contains the MOC Image Numbers of all the images in the Gusev Crater Landing site area for this study.

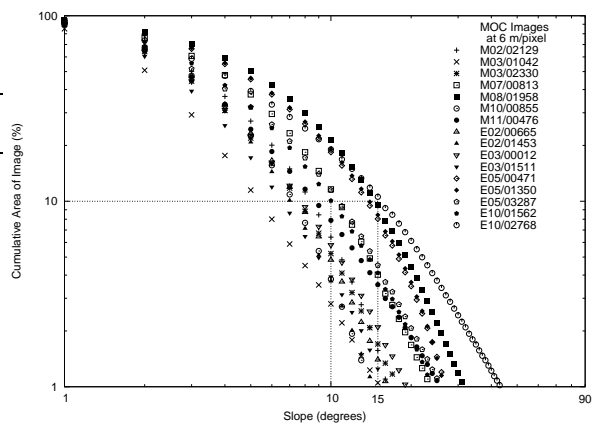


Figure 23: Gusev Crater Site Slope Distribution.

4 Application to MER 2003 Landing Sites

The point photogrammetry technique that we used in this study is not yielding exact slope measurements, due to the albedo variations and coarse haze estimations that we employed. However, by conservatively measuring the images and using the au-

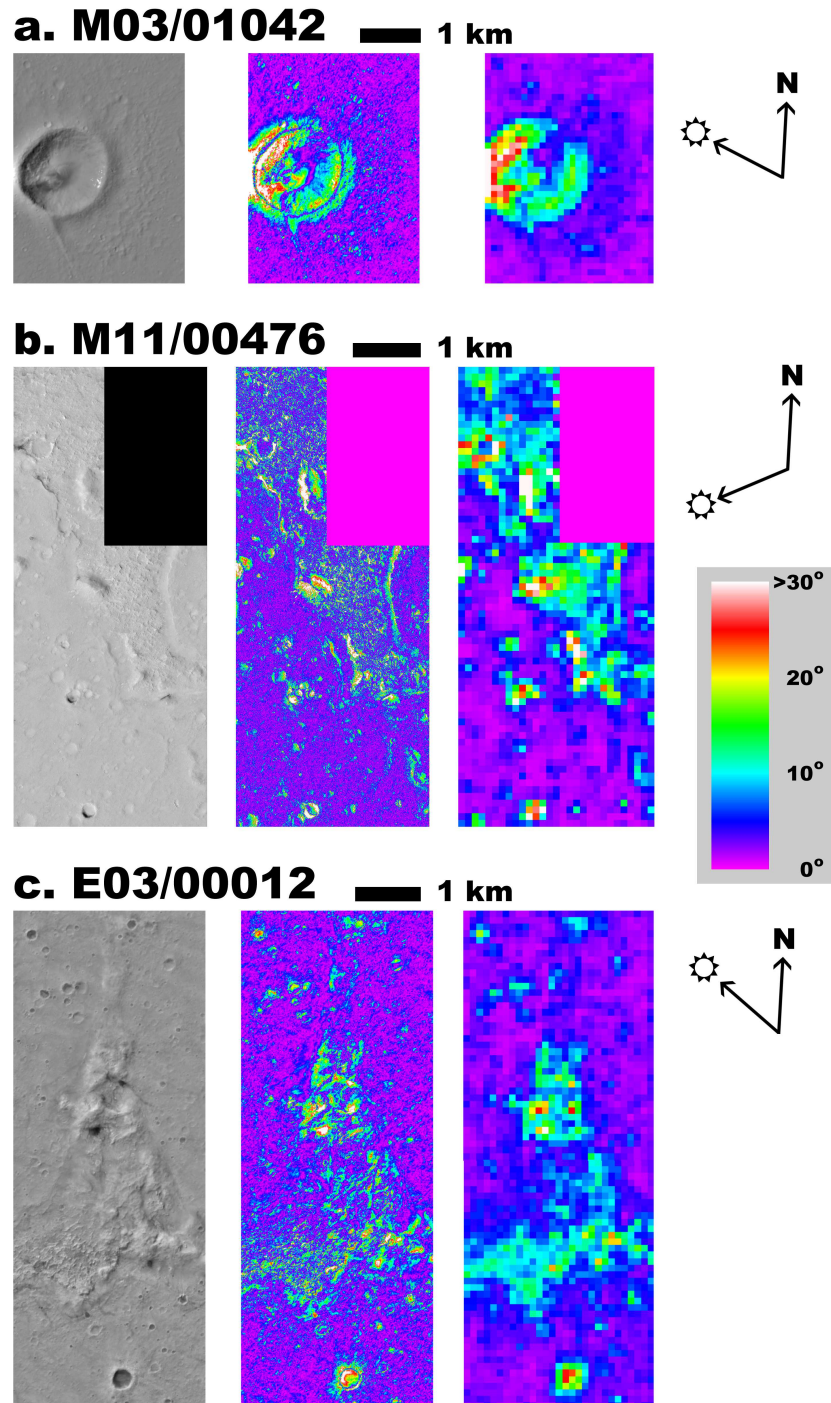


Figure 24: Each of these three figures contain a portion of a cleaned and calibrated MOC image in the Gusev Crater study area, a slope image at the original resolution of the MOC image, and an RMS slope image. The large pixels in the RMS slope image are 100 m across. (a) Portion of M03/01042. This image shows the slopes on a large crater in the Gusev ellipse. (b) Portion of M11/00476. This image shows the rougher slopes of an etched unit. (c) Portion of E03/00012. This image shows the slopes of a triangular hill identified as a basin floor unit.

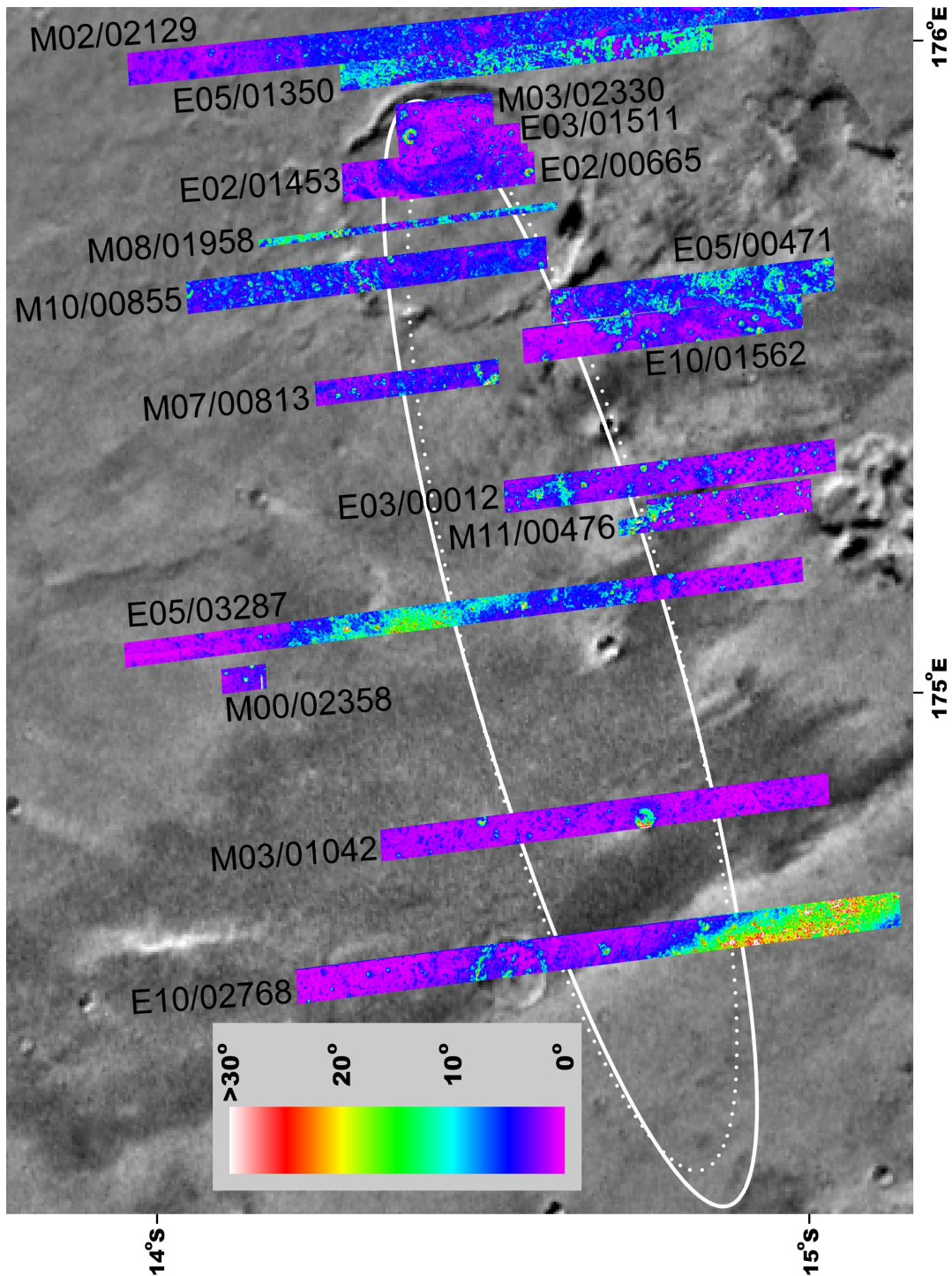


Figure 25: Gusev Crater RMS Slope Image Mosaic. The colored RMS slope images of the various MOC images in this area are mosaicked onto a basemap of Viking Orbiter images (MDIM 2). The solid ellipse is the location of the landing ellipse at the opening of the launch window, and the dotted ellipse is the location at the close of the launch window.

Isidis MOC Image Number	Planitia Resolution (m/pixel)	Landing Incidence Angle (°)	Site Portion Measured
M10/01982	7.244	39.92	central
M21/00723	2.905	37.32	northern
E02/00049	5.85	39.13	all
E02/00681	2.94	38.86	southern
E02/02211	2.936	38.34	all
E03/00038	2.93	38.63	southern
E03/01529	2.92	38.69	southern
E04/01562	2.925	39.27	all
E05/00486	2.928	39.83	all
E05/02100	2.914	40.51	all
E09/00789	6.117	41.91	all
E11/00717	3.051	36.57	all
E11/02075	3.055	35.48	northern
E12/00438	3.059	31.75	all
E12/01266	3.055	30.53	all
E12/02073	1.482	29.89	all
E13/00145	3.243	28.38	all
E13/00788	3.317	27.45	all
E13/01415	1.959	27.47	all
E13/02262	3.056	23.58	all
E14/02034	1.525	21.09	all
E16/01402	3.046	23.30	all
E16/01980	3.052	24.12	all
E17/01666	3.047	28.04	all
E18/00196	3.05	28.98	all
E18/00622	3.053	29.94	all
E18/01521	1.463	32.11	all

Table 11: This table contains the MOC Image Numbers of all the images in the Isidis Planitia Landing site area for this study.

tomatic maximum haze estimation we were able to yield a solid upper bound to the down-sun slopes in the images measured. The slope values reported by our photoclinometry measurement technique should not be looked at in isolation, we strongly suggest that our slope measurements be one more piece of information on which to judge the safety of any given landing ellipse, and that they not be considered without also looking at the images that were measured to create them.

4.1 Athabasca Valles

We found twenty-four images that overlapped the potential landing area in Athabasca Valles, listed in Table 7. The slope statistics for Athabasca can be

found in Figures 11 and 12.

The Athabasca Valles site was eliminated from consideration for MER 2003 due to high radar backscatter values in the area, but continues to be an interesting area for study and a possible destination for future landers (*Burr et al., 2002*).

The mosaic of RMS slope images in Figure 13 shows how these RMS slope images are useful indicators of morphologic change on the surface. The images in the western portion of the proposed landing ellipse show rather smooth terrain, with groupings of fresh looking craters adding some roughness. A small dunefield is picked out in the RMS slope image of M04/02002. The high-slope area in the southern portion of E13/00030 is a high-standing ridge. There is some rough terrain in the southern portions of E11/03799 and E13/01475 that is highlighted by the RMS slope images. The interior slope of the crater at the southern end of E12/01728 (Figure 14a) is easily seen in the RMS slope images as is the steeper slope of its eroded northern flank. The RMS slope images in the eastern portion of the ellipse (e.g. Figures 14b and 14c) display steep slopes associated with the sides of streamlined mesas, and scour marks on the floors of the channels (*Burr et al., 2002*). Additionally, some of the roughness images clearly delineate the smoother channel floor from the slightly rougher banks (e.g. E12/01746 and E10/02604).

4.2 Elysium Planitia

The landing site in Elysium Planitia was added into the site selection process after the Athabasca Valles and Melas Chasma sites were eliminated, and so MOC coverage of this area was limited at the time of our study. The images we measured are listed in Table 8, and the measurements are in Figures 15 and 16.

The RMS slope images in this area (Figure 17a) mostly show the presence of craters. The roughness in the RMS slope image of E18/01327 (Figure 18a) is due to low albedo and a number of small, fresh craters. Other large craters are easy to observe in the various RMS slope images. A ridge running south from a large crater in E18/00429 (Figure 18b) is highlighted by its steeper slopes. A crater rim and its rays are displayed in the RMS slope image of E18/00019 (Figure 18c), and the slope information also displays a low ridge running east-west along the northern border of the ellipse.

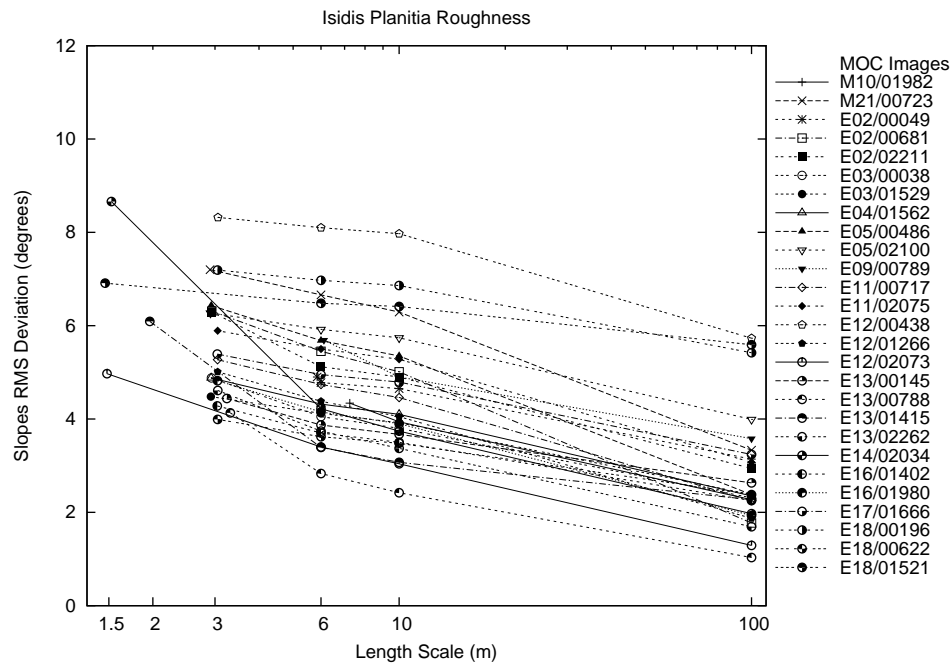


Figure 26: Isidis Planitia Site RMS Roughness.

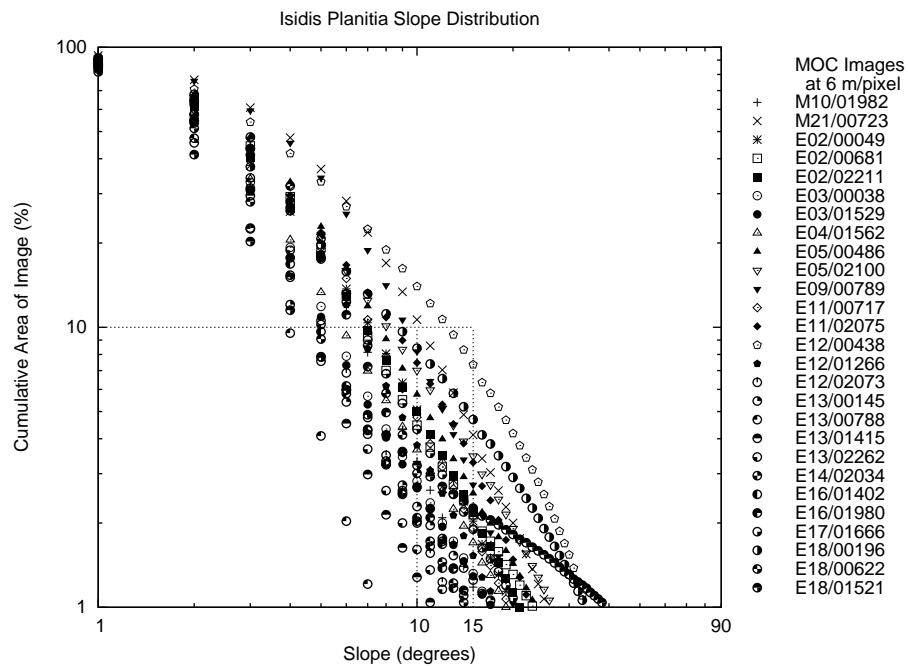


Figure 27: Isidis Planitia Site Slope Distribution at 6m/pixel.

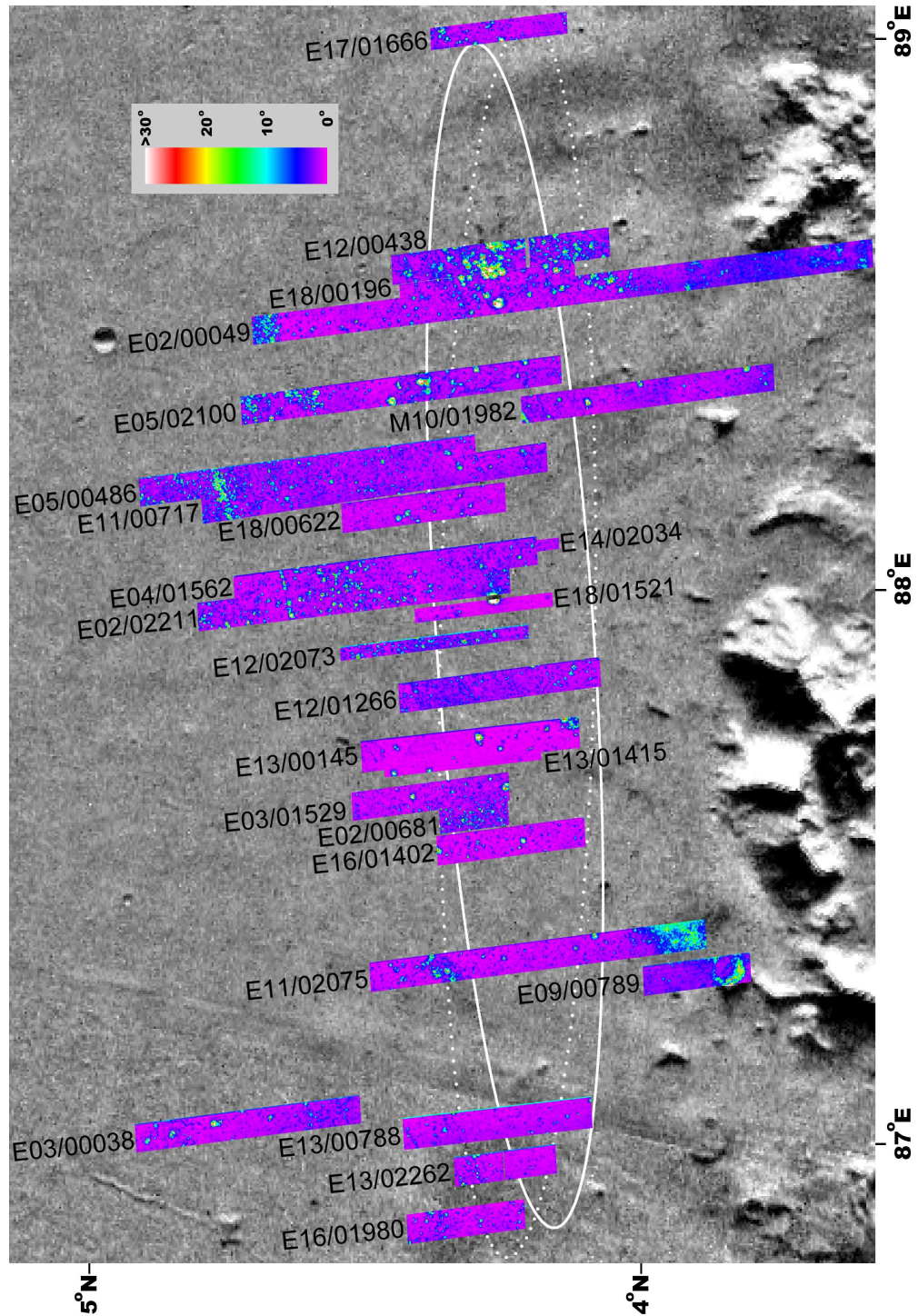


Figure 28: Isidis Planitia RMS Slope Image Mosaic. The colored RMS slope images of the various MOC images in this area are mosaicked onto a basemap of Viking Orbiter images (MDIM 2). The solid ellipse is the location of the landing ellipse at the opening of the launch window, and the dotted ellipse is the location at the close of the launch window.

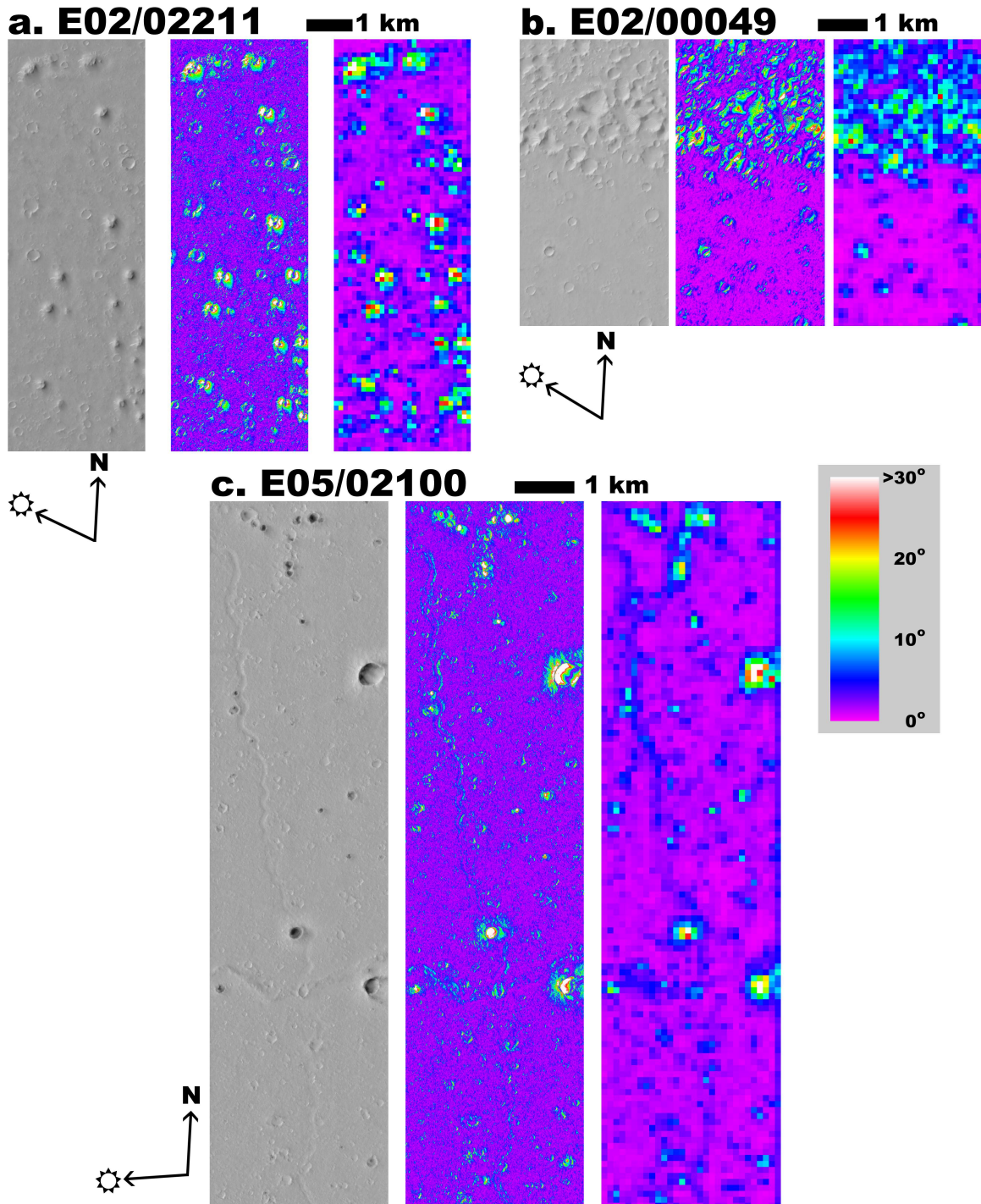


Figure 29: Each of these three figures contain a portion of a cleaned and calibrated MOC image in the Isidis Planitia study area, a slope image at the original resolution of the MOC image, and an RMS slope image. The large pixels in the RMS slope image are 100 m across. (a) Portion of E02/02211. Outside of the ellipse the slopes of small, scattered hillocks can be seen in the slope images. (b) Portion of E02/00049. This portion of the image outside of the ellipse shows a concentration of small, closely spaced craters. (c) Portion of E05/02100. The slopes of a small channel that runs north-south within the ellipse can be seen in the slope images.

Meridiani Planum Landing Site Images

MOC Image Number	Resolution (m/pixel)	Incidence Angle (°)	Portion Measured
M00/01660	1.432	42.77	all
M03/01632	5.765	40.73	northern
M08/02647	1.442	40.19	all
M08/08066	2.886	39.55	all
E01/01056	2.9	43.0	northern
E02/00970	2.92	42.25	southern
E03/00329	2.91	41.56	central
E03/01763	2.9	41.15	central
E04/01682	3.3	42.74	central
E04/01873	2.92	40.55	central
E05/00801	2.91	40.50	all
E05/02642	2.90	40.51	all
E10/00916	6.08	36.90	all

Table 12: This table contains the MOC Image Numbers of all the images in the Meridiani Planum Landing site area for this study.

4.3 Eos Chasma

There were seventeen images that have sections within the Eos Chasma landing ellipse (see Table 9). Since most of the images contain terrain that climbs up the chasma walls to the north or south, we did not measure the ends of most of the images. The statistical information for the Eos Chasma images are in Figures 19 and 20.

Eos Chasma was eliminated from the site selection process due to slope winds that sweep up and down the walls of the Valles Marineris, making this area quite dangerous for the MER 2003 afternoon landing.

The mosaic of RMS slope images in Figure 17b shows how these RMS slope images are useful indicators of morphologic change. The slopes on the tail of the streamlined landform to the west of the ellipse can be seen in the RMS slope images of E04/00506 (Figure 21a) and M03/00926. Additionally, some of the hummocky terrain to the southeast of the ellipse can be seen in the RMS slope images of E03/01452 (Figure 21b), M02/02072, and E02/00633 (Figure 21c). Aside from crater forms within the proposed ellipse, there does not seem to be other distinctive morphologies within the ellipse.

4.4 Gusev Crater

The images in Table 10 are in or near the Gusev Crater landing ellipse (*Cabrol et al., 2003*). The floor of Gusev Crater presents some problems for our photogrammetry technique in the form of large dark-toned areas made up of dust-devil tracks and wind streaks (*Milam et al., 2003*). The southern half of M07/00813 was not measured, because of these albedo problems. However, other images in this area were not as severely affected. Figures 22 and 23 show the slope statistics for these images in Gusev Crater.

The slope signature of large craters is evident in the RMS slope images of E10/02768, M03/01042 (Figure 24a), and M03/02330. The southern patch of the Etched unit (ET) identified by *Milam et al. (2003)* in the center of the ellipse is easily seen in the RMS slope image of M11/00476 (Figure 24b). Additionally, the rougher slopes of the larger ET unit can be seen in the RMS slope images of E10/01562 and E05/00471. The RMS slope image of E03/00012 (Figure 24c) distinctly shows a triangular patch of material with steeper slopes that corresponds to an island of Basin Floor unit 1 (AHbm1) identified by *Kuzmin et al. (2000)*.

In the context of the RMS slope image mosaic (Figure 25), the rim of the Thira crater and the rougher terrain outside of it can be seen in the RMS slope images on the eastern end of the ellipse. Additionally, many of the different units identified in the hazard map of *Golombek et al. (2003)* for Gusev crater can also be identified in this mosaic by changes in roughness for the different units.

4.5 Isidis Planitia

There were twenty-seven images (Table 11) in the Isidis Planitia Landing ellipse (*Crumpler and Tanaka, 2003*). This site also had very low roughness, as the maximum slope measurements in Figures 26 and 27 show.

The distribution of slopes within the Isidis ellipse is shown in Figure 28. The RMS slope images here are mostly picking out large craters. There are a number of dark-floored craters in this region. Because of the low-albedo material on their floors, our photogrammetry technique indicates that their floors are very steep, making these craters very obvious on the RMS slope images (and potentially inflating the slope statistics). Good examples are in the southern

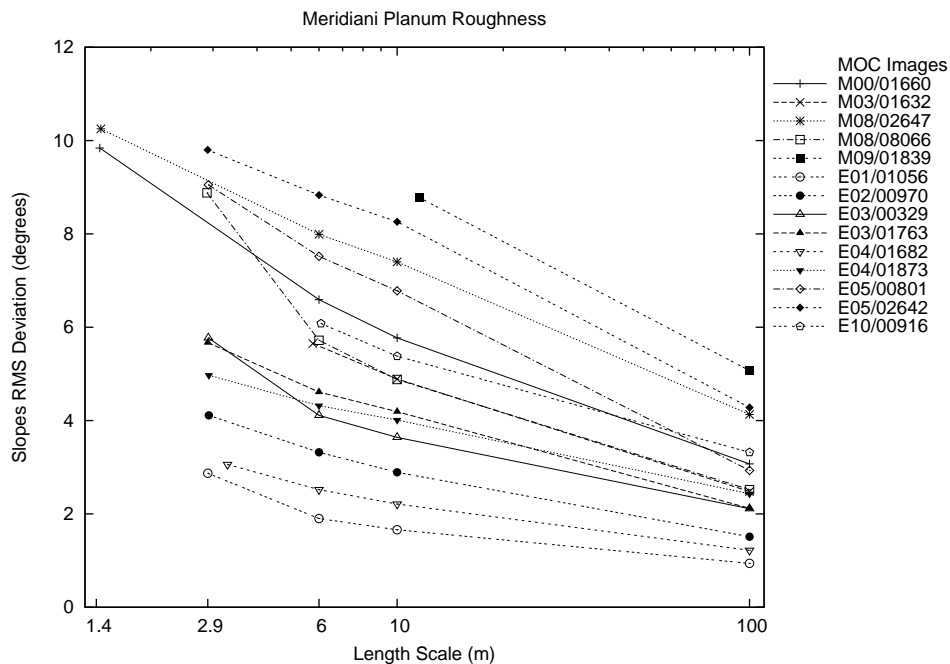


Figure 30: Meridiani Planum RMS Roughness.

tip of E13/00145, E18/00622, and within the ellipse on E18/00196 and E12/00438. However, the areas that have steep slopes in the mosaic are consistent with areas on the hazard maps of *Golombek et al.* (2003) that have fresh craters and heavily cratered terrain. The northern portions of the RMS slope images of E02/02211 (Figure 29a) and E04/01562 display a freckled pattern of high slopes, that correspond to some small hillocks north of the ellipse. There is a band of closely spaced craters with high-albedo dunes on their floors that show up nicely in the northern portions of the RMS slope images of E11/00717 and E05/00486. Terrain similar to this in appearance and slope characteristics appears in the northern tips of E05/02100 and E02/00049 (Figure 29b). The RMS slope image of E05/02100 (Figure 29c) nicely displays a shallow channel that runs north-south and bisects the southern portion of that image within the ellipse.

4.6 Melas Chasma

The MOC images of the Melas Chasma landing site (*Weitz et al.*, 2003) had too many albedo variations to make application of our photoclinometry tech-

nique practical. The images showed areas of high contrast albedo variation that did not appear slope-related. There were light-toned areas that probably are rough, but they effectively saturated the technique (reported slopes were around 90°), making accurate measurement impossible. There were albedo variations which were 0.5 to 1 km across that may or may not be topographic, some appeared to be mesas. There were also areas that seemed to have dark dust or sand that have filled in the lows of what appear to be indurated dunes or grooves. This area is of geologic interest, but we felt it constituted terrain that is dangerous to the MER landing system. Other researchers felt the same way, and the Melas Chasma site has been eliminated for MER 2003, but remains an attractive target for future study.

4.7 Meridiani Planum

The ellipse in Meridiani Planum is situated such that it sits within the area identified as having Hematite spectral characteristics (*Christensen et al.*, 2000). We measured thirteen MOC images that overlap the ellipse in Meridiani Planum (Table 12). The MOC images of this area show that it is dominated by

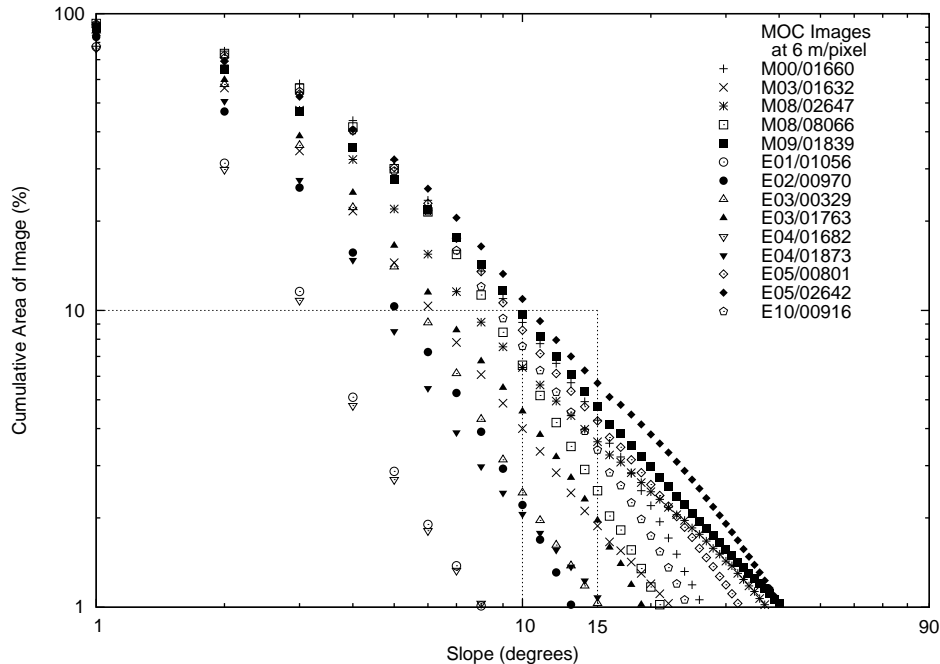


Figure 31: Meridiani Planum Slope Distribution.

two kinds of albedo variations. One is what appears to be a rocky or indurated surface that has been cleaned or scoured of dust. This leaves a light-toned surface of high contrast that is rough, but probably not as rough as our algorithm reports. The other albedo pattern is that of buried or exhumed craters (Arvidson *et al.*, 2003).

Despite the complication of these persistent albedo variations, the RMS slope distributions and cumulative area measurements in Figures 30 and 31 show that this area is relatively smooth. When the albedo variations are considered, this area is probably smoother than these measurements suggest (as discussed above in §3.2).

In looking at the mosaic of RMS slope images (Figure 32) for this potential landing ellipse, most of the model slopes greater than 10° are the result of high-albedo rough areas and the characteristic albedo pattern of the exhumed craters. This pattern is a light-toned signature of the rim and a dark-toned patch at the center where dark material seems to have collected. Additionally, there are often light-toned, high-contrast dune fields in the centers of these craters. An example of this typical pattern can be found in the E05/00801 image (Figure 33a).

The images in the mosaic also highlight fresh and degraded craters identified by Golombek *et al.* (2003) in their Meridiani Planum hazard map.

The RMS slope image of E02/00970 (Figure 33b) nicely identifies the rays and flank of a fresh-looking crater. The RMS slope images of M09/01839 (Figure 33c) and E04/01873 show some craters that have steeper model slopes than other exhumed craters in this area. There are two in M09/01839, one just north of the ellipse and another that is within the ellipse, they have rims that appear to stand above the terrain and have some real topography to them, indicating that they are not as deeply buried as other exhumed craters in this area. The crater in E04/01873 south of the ellipse has a rim which can be seen much more clearly than other buried craters in this area indicating that it may be at a different stage of burial or exhumation.

5 Conclusions

Our technique allowed us to measure slope characteristics at the meter scale for six of the candidate landing sites, and show that all had slope characteristics within the acceptable constraints for

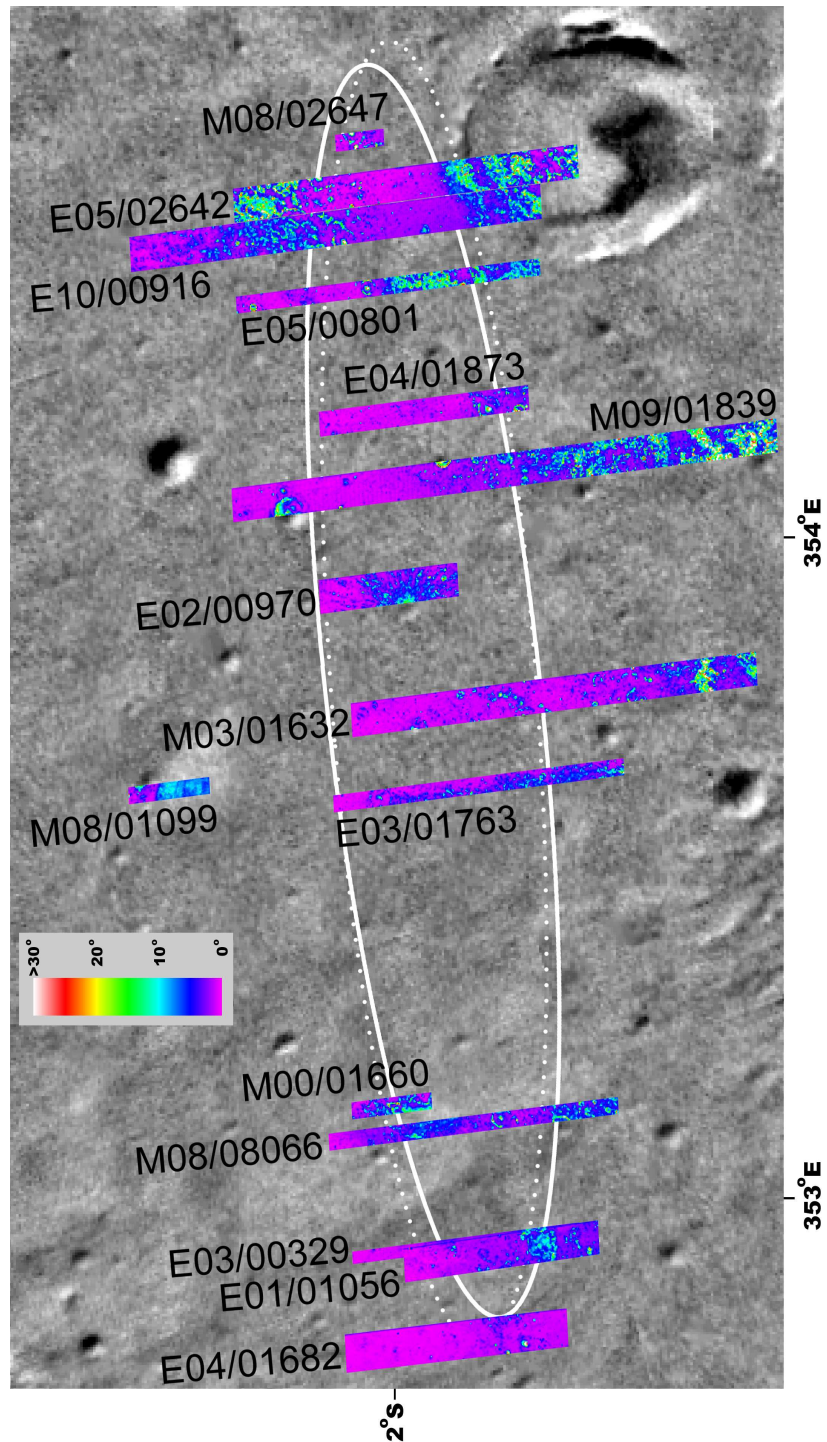


Figure 32: Meridiani Planum RMS Slope Image Mosaic. The colorized RMS slope images of the various MOC images in this area are mosaicked onto a basemap of Viking Orbiter images (MDIM 2). The solid ellipse is the location of the landing ellipse at the opening of the launch window, and the dotted ellipse is the location at the close of the launch window.

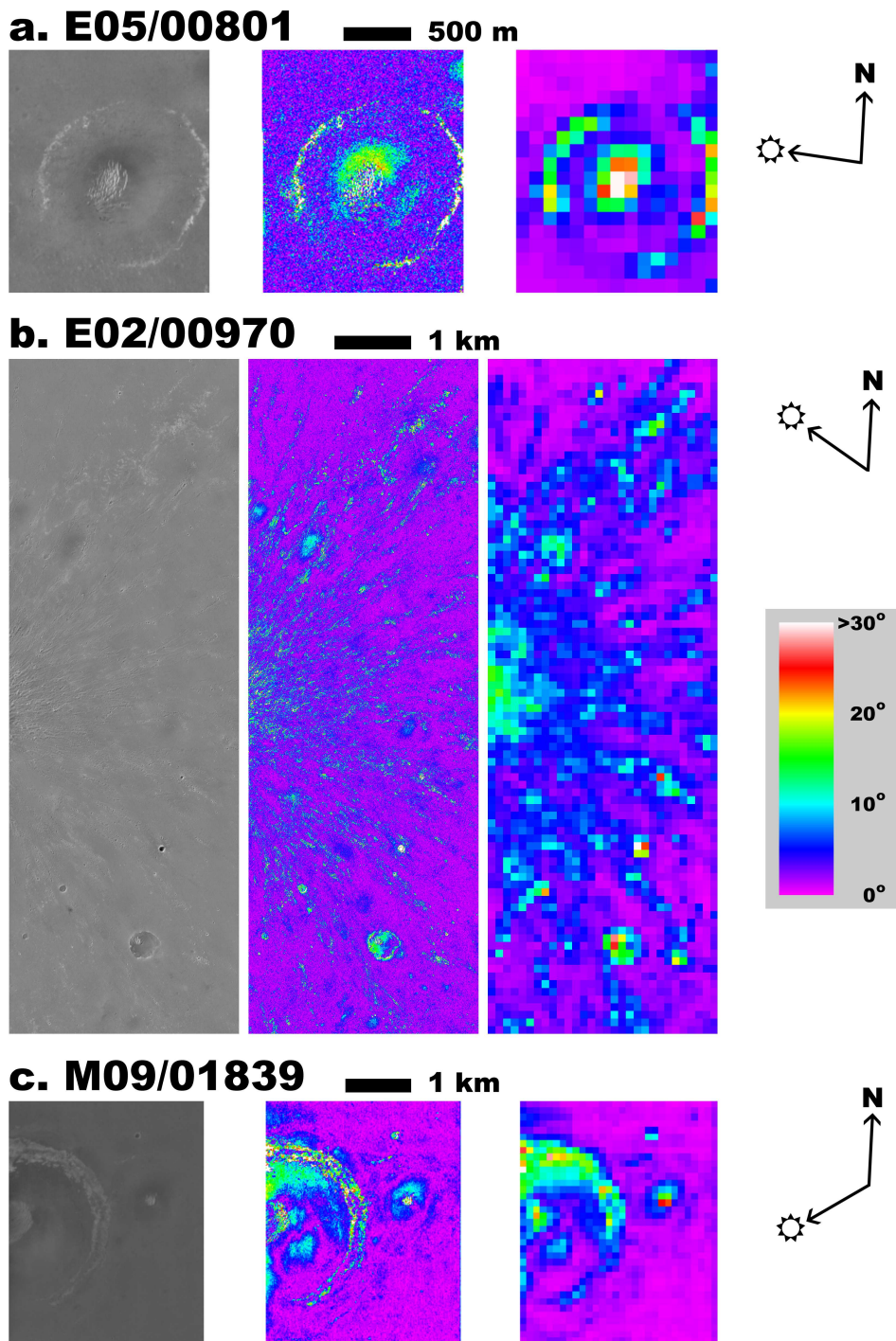


Figure 33: Each of these three figures contain a portion of a cleaned and calibrated MOC image in the Meridiani Planum study area, a slope image at the original resolution of the MOC image, and an RMS slope image. The large pixels in the RMS slope image are 100 m across. (a) Portion of E05/00801. This image shows a typical exhumed crater in the Meridiani Planum area. (b) Portion of E02/00970. This image picks out the rougher rays and flank of a crater. (c) Portion of M09/01839. This image shows another exhumed crater, but this one's rim appears a little more raised than others, and the rim also appears a little differently eroded.

the MER 2003 landers. Our point photogrammetry method performed well on synthetic topography, and agreed well with results from area photogrammetry and stereogrammetry. It also passed the test of ground truth at the landing sites of Viking 1, Viking 2, and Pathfinder. By measuring several images in the same area, we were able to catch blatant outliers in the automatic estimation of haze. Due to the severe albedo variations in Melas Chasma, we were unable to obtain reliable slope measurements. However, the topography in the images near the Melas Chasma site appears to contain mesas and other obstacles that present an obvious hazard to the MER 2003 landers.

Our method in this study provides an upper bound to the down-sun slope statistics of the images, not a true slope measurement. However, we have shown that when a more refined haze estimate for an image is available, our technique is able to provide more accurate slope statistics (e.g. when we compared area photogrammetry to our technique in §3.2). Additionally, our method is able to operate on and process a large number of images rather quickly, which allows us to complement and extend slope information from area photogrammetry and stereogrammetry.

The final slope criterion for site selection was based on an area-weighted failure rate of Monte Carlo entry, descent, and landing simulations based on the DEMs of *Kirk et al.* (2003). However, having extensive maps of roughness estimates that are internally consistent even if they are produced differently from the DEMs is the proper basis for assigning the area weights to the outcomes of the simulations based on the area-restricted DEMs. Additionally, these statistics can be produced to allow initial comparison of sites before the Monte Carlo results are complete.

This technique is ideal for landing site evaluation both in the early stages of site selection when there are large numbers of landing ellipses to choose from, and in the latter stages when slope information from as much terrain within a particular landing ellipse is needed and is not available from other methods.

A Software Used

We primarily used the USGS ISIS software (version 010515) (*Eliason et al.*, 2001; *Gaddis et al.*, 1997) in this study for our image processing. Initial pro-

cessing involved the use of the `moclev0` and `moclev1` procedures. Photometric information was extracted from the level 1 image via the `lev1pt` program. The various boxcar filtering operations were performed using the `boxfilter` procedure in both `DIVIDE` and `LPF` modes. Resolution degradations were performed with `magcube`.

All tasks having to do with transforming brightness information into slope measurements were performed with a program written specifically for this task in the C++ programming language.

B Differences from the Version Published by AGU

As noted on the first page, this paper was originally published by the AGU. The differences between the paper published by the AGU and this document are essentially those of formatting. The text, figures and tables are identical (with the exception that this version correctly uses the term Orbiter instead of Orbital for the ‘O’ in both MOC and MOLA in the Introduction), and this appendix has been added.

Even though the American Geophysical Union owns the copyright for this work, I have self-archived this paper by placing it on my own personal web site (under the terms outlined by the AGU) as an exercise of one of the nonexclusive rights granted to me as an author of the work from the AGU under the copyright transfer agreement that transferred the copyright from me to the AGU.

These rights are described on the “AGU Permissions and Copyright Information” page, dated 22 September 2004, posted on the Web by AGU at http://www.agu.org/pubs/cprt_top.html.

To learn more about self-archiving and open access, visit the Self-Archiving FAQ at <http://www.eprints.org/self-faq/> and the Budapest Open Access Initiative at <http://www.soros.org/openaccess/>.

Acknowledgements. We would like to thank Albert Haldemann and an anonymous reviewer for insightful and constructive reviews of this paper. This research has made use of NASA’s Astrophysics Data System. Funding support for R. A. Beyer and A. S. McEwen came from the Mars Characterization for Future Missions program (JPL/MGS and NASA/MDAP).

References

- Acton, C. H., Ancillary data services of NASA's Navigation and Ancillary Information Facility, *Planetary and Space Science*, *44*, 65–70, 1996.
- Acton, C. H., SPICE Products Available to the Planetary Science Community, in *Lunar and Planetary Science XXX*, #1233, Lunar and Planetary Institute, Houston (CD-ROM), 1999.
- Arvidson, R. E., F. P. Seelos, K. S. Deal, W. C. Koeppen, N. O. Snider, J. M. Kieniewicz, B. M. Hynek, M. T. Mellon, and J. B. Garvin, Mantled and exhumed terrains in Terra Meridiani, Mars, *Journal of Geophysical Research*, *108*, 14–1, 2003.
- Binder, A. B., R. E. Arvidson, E. A. Guinness, K. L. Jones, T. A. Mutch, E. C. Morris, D. C. Pieri, and C. Sagan, The geology of the Viking Lander 1 site, *Journal of Geophysical Research*, *82*, 4439–4451, 1977.
- Burr, D. M., J. A. Grier, A. S. McEwen, and L. P. Keszthelyi, Repeated Aqueous Flooding from the Cerberus Fossae: Evidence for Very Recently Extant, Deep Groundwater on Mars, *Icarus*, *159*, 53–73, 2002.
- Cabrol, N. A., E. A. Grin, M. H. Carr, B. Sutter, J. M. Moore, J. D. Farmer, R. Greeley, R. O. Kuzmin, D. J. DesMarais, M. G. Kramer, H. Newsom, C. Barber, I. Thorsos, K. L. Tanaka, N. G. Barlow, D. A. Fike, M. L. Urquhart, B. Grigsby, F. D. Grant, and O. de Goursac, Exploring Gusev Crater with Spirit: Review of science objectives and testable hypotheses, *Journal of Geophysical Research*, *108*, 17–1, 2003.
- Christensen, P. R., J. L. Bandfield, R. N. Clark, K. S. Edgett, V. E. Hamilton, T. Hoefen, H. H. Kieffer, R. O. Kuzmin, M. D. Lane, M. C. Malin, R. V. Morris, J. C. Pearl, R. Pearson, T. L. Roush, S. W. Ruff, and M. D. Smith, Detection of crystalline hematite mineralization on Mars by the Thermal Emission Spectrometer: Evidence for near-surface water, *Journal of Geophysical Research*, *105*, 9623–9642, 2000.
- Crisp, J. A., M. Adler, J. R. Matijevic, S. W. Squyres, R. E. Arvidson, and D. M. Kass, Mars Exploration Rover mission, *Journal of Geophysical Research*, *108*, 2–1, 2003.
- Crumpler, L. S., and K. L. Tanaka, Geology and MER target site characteristics along the southern rim of Isidis Planitia, Mars, *Journal of Geophysical Research*, *108*, 21–1, 2003.
- Eliason, E. M., J. A. Anderson, J. M. Barrett, K. J. Becker, T. L. Becker, D. A. Cook, L. A. Soderblom, T. L. Sucharski, and K. T. Thompson, ISIS Image Processing Capabilities for MGS/MOC Imaging Data, in *Lunar and Planetary Science XXXII*, #2081, Lunar and Planetary Institute, Houston (CD-ROM), 2001.
- Gaddis, L., J. Anderson, K. Becker, T. Becker, D. Cook, K. Edwards, E. Eliason, T. Hare, H. Kieffer, E. M. Lee, J. Mathews, L. Soderblom, T. Sucharski, J. Torson, A. McEwen, and M. Robinson, An Overview of the Integrated Software for Imaging Spectrometers (ISIS), in *Lunar and Planetary Science Conference*, vol. 28, p. 387, 1997.
- Garvin, J. B., J. J. Frawley, and J. B. Abshire, Vertical roughness of Mars from the Mars Orbiter Laser Altimeter, *Geophysical Research Letters*, *26*, 381–384, 1999.
- Golombek, M. P., H. J. Moore, A. F. C. Haldemann, T. J. Parker, and J. T. Schofield, Assessment of Mars Pathfinder landing site predictions, *Journal of Geophysical Research*, *104*, 8585–8594, 1999.
- Golombek, M. P., J. A. Grant, T. J. Parker, D. M. Kass, J. A. Crisp, S. W. Squyres, A. F. C. Haldemann, M. Adler, W. J. Lee, N. T. Bridges, R. E. Arvidson, M. H. Carr, R. L. Kirk, P. C. Knocke, R. B. Roncoli, C. M. Weitz, J. T. Schofield, R. W. Zurek, P. R. Christensen, R. L. Fergason, F. S. Anderson, and J. W. Rice, Selection of the Mars Exploration Rover landing sites, *Journal of Geophysical Research*, *108*, 13–1, 2003.
- Haldemann, A. F., and F. S. Anderson, Mars Exploration Rover Landing Site Hectometer Slopes, in *American Geophysical Union, Fall Meeting*, #P22A-0390, 2002.
- Kirk, R. L., E. Howington-Kraus, T. Hare, E. Dorner, D. Cook, K. Becker, K. Thompson, B. Redding, J. Blue, D. Galuszka, E. M. Lee, L. R. Gaddis, J. R. Johnson, L. A. Soderblom, A. W. Ward, P. H. Smith, and D. T. Britt, Digital photogrammetric analysis of the IMP camera images: Map-

- ping the Mars Pathfinder landing site in three dimensions, *Journal of Geophysical Research*, *104*, 8869–8888, 1999.
- Kirk, R. L., K. T. Thompson, T. L. Becker, and E. M. Lee, Photometric Modeling for Planetary Cartography, in *Lunar and Planetary Science XXXII*, #2025, pp. 2025–+, Lunar and Planetary Institute, Houston (CD-ROM), 2000.
- Kirk, R. L., K. T. Thompson, and E. M. Lee, Photometry of the Martian Atmosphere: An Improved Practical Model for Cartography and Photoclinometry, in *Lunar and Planetary Science XXXII*, #1874, Lunar and Planetary Institute, Houston (CD-ROM), 2001.
- Kirk, R. L., E. Howington-Kraus, B. Redding, D. Galuszka, T. M. Hare, B. A. Archinal, L. A. Soderblom, and J. M. Barrett, High-resolution topomapping of candidate MER landing sites with Mars Orbiter Camera narrow-angle images, *Journal of Geophysical Research*, *108*, 29–1, 2003.
- Kuzmin, R. O., R. Greeley, R. Landheim, N. A. Cabrol, and J. D. Farmer, *Geologic Map of the MTM-15182 and MTM-15187 Quadrangles, Gusev Crater-Ma'adim Vallis Region, Mars*, United States Geologic Survey, 2000.
- Malin, M. C., and K. S. Edgett, Mars Global Surveyor Mars Orbiter Camera: Interplanetary cruise through primary mission, *Journal of Geophysical Research*, *106*, 23,429–23,570, 2001.
- McEwen, A. S., Exogenic and endogenic albedo and color patterns on Europa, *Journal of Geophysical Research*, *91*, 8077–8097, 1986.
- McEwen, A. S., Photometric functions for photoclinometry and other applications, *Icarus*, *92*, 298–311, 1991.
- Milam, K. A., K. R. Stockstill, J. E. Moersch, H. Y. McSween, L. L. Tornabene, A. Ghosh, M. B. Wyatt, and P. R. Christensen, THEMIS characterization of the MER Gusev Crater landing site, *Journal of Geophysical Research*, *108*, 19–1, 2003.
- Minnaert, M., The reciprocity principle in lunar photometry, *Astrophys. J.*, *93*, 403–410, 1941.
- Morris, E. C., and K. L. Jones, Viking 1 Lander on the surface of Mars - Revised location, *Icarus*, *44*, 217–222, 1980.
- Mutch, T. A., R. E. Arvidson, E. A. Guinness, A. B. Binder, and E. C. Morris, The geology of the Viking Lander 2 site, *Journal of Geophysical Research*, *82*, 4452–4467, 1977.
- Neumann, G. A., J. B. Abshire, O. Aharonson, J. B. Garvin, X. Sun, and M. T. Zuber, Mars Orbiter Laser Altimeter pulse width measurements and footprint-scale roughness, *Geophysical Research Letters*, *30*, 15–1, 2003.
- Oberst, J., W. Zeitler, and M. Kuschel, Where is Viking Lander 2?, in *Lunar and Planetary Science XXXI*, #1612, Lunar and Planetary Institute, Houston (CD-ROM), 2000.
- Parker, T. J., and R. L. Kirk, Location and Geologic Setting for the Three U.S. Mars Landers, in *Fifth International Conference on Mars*, #6124, Lunar and Planetary Institute, Houston (CD-ROM), 1999.
- Parker, T. J., R. L. Kirk, and M. E. Davies, Location and Geologic Setting for the Viking 1 Lander, in *Lunar and Planetary Science XXX*, #2040, Lunar and Planetary Institute, Houston (CD-ROM), 1999.
- Shepard, M. K., B. A. Campbell, M. H. Bulmer, T. G. Farr, L. R. Gaddis, and J. J. Plaut, The roughness of natural terrain: A planetary and remote sensing perspective, *Journal of Geophysical Research*, *106*, 32,777–32,796, 2001.
- Shorthill, R. W., R. E. Hutton, H. J. Moore, R. F. Scott, and C. R. Spitzer, Physical properties of the Martian surface from the Viking 1 lander - Preliminary results, *Science*, *193*, 805–809, 1976a.
- Shorthill, R. W., H. J. Moore, R. E. Hutton, R. F. Scott, and C. R. Spitzer, The environs of Viking 2 lander, *Science*, *194*, 1309–1318, 1976b.
- Smith, D. E., M. T. Zuber, H. V. Frey, J. B. Garvin, J. W. Head, D. O. Muhleman, G. H. Pettengill, R. J. Phillips, S. C. Solomon, H. J. Zwally, W. B. Banerdt, T. C. Duxbury, M. P. Golombek, F. G. Lemoine, G. A. Neumann, and et al., Mars Orbiter Laser Altimeter: Experiment summary after the first year of global mapping of Mars, *Journal of Geophysical Research*, *106*, 23,689–23,722, 2001.
- Smith, P. H., J. F. Bell, N. T. Bridges, D. T. Britt, L. Gaddis, R. Greeley, H. U. Keller, K. E. Herkenhoff, R. Jaumann, J. R. Johnson, R. L. Kirk,

- M. Lemmon, J. N. Maki, M. C. Malin, S. L. Murchie, J. Oberst, T. J. Parker, R. J. Reid, R. Sablotny, L. A. Soderblom, C. Stoker, R. Sullivan, N. Thomas, M. G. Tomasko, W. Ward, and E. Wegryn, Results from the Mars Pathfinder Camera, *Science*, 278, 1758, 1997.
- Soderblom, L. A., R. L. Kirk, and K. E. Herkenhoff, Accurate Fine-Scale Topography for the Martian South Polar Region from Combining MOLA Profiles and MOC NA Images, in *Lunar and Planetary Science XXXIII*, #1254, Lunar and Planetary Institute, Houston (CD-ROM), 2002.
- Turcotte, D. L., *Fractals and Chaos in Geology and Geophysics*, Cambridge University Press, New York, 1997.
- Ward, A. W., L. R. Gaddis, R. L. Kirk, L. A. Soderblom, K. L. Tanaka, M. P. Golombek, T. J. Parker, R. Greeley, and R. O. Kuzmin, General geology and geomorphology of the Mars Pathfinder landing site, *Journal of Geophysical Research*, 104, 8555–8572, 1999.
- Weitz, C. M., T. J. Parker, M. H. Bulmer, F. Scott Anderson, and J. A. Grant, Geology of the Melas Chasma landing site for the Mars Exploration Rover mission, *Journal of Geophysical Research*, 108, 23–1, 2003.
- Zeitler, W., and J. Oberst, The Mars Pathfinder landing site and the Viking control point network, *Journal of Geophysical Research*, 104, 8935–8942, 1999.

Ross A. Beyer and Alfred S. McEwen, Department of Planetary Sciences, The University of Arizona, Kuiper Space Sciences Building, Tucson, AZ 85721-0092, USA. (rbeyer@lpl.arizona.edu and mcewen@lpl.arizona.edu)

Randolph L. Kirk, Astrogeology Team, U.S. Geological Survey, 2255 N. Gemini Dr., Flagstaff, AZ 86001, USA. (rkirk@usgs.gov)